Research Square

Preprints are preliminary reports that have not undergone peer review.
They should not be considered conclusive, used to inform clinical practice,
or referenced by the media as validated information.

Dynamic Response and Joint Wear Characteristics of a Rigid–Flexible Coupled High-Frequency Flapping-Wing Mechanism with Revolute Joint Clearances

Yunfang Lv

19051697635@163.com

Shandong University of Science and Technology

Research Article

Keywords: high-frequency flapping-wing mechanism, revolute joint clearance, rigid–flexible coupling, dynamic response, wear characteristics

Posted Date: October 12th, 2026

DOI: https://doi.org/10.21203/rs.3.rs-11043576/v1

License: This work is licensed under a Creative Commons Attribution 4.0 International License.
Read Full License

Additional Declarations: No competing interests reported.

Dynamic Response and Joint Wear Characteristics of a Rigid–Flexible Coupled High-Frequency Flapping-Wing Mechanism with Revolute Joint Clearances

Yunfang Lv[1]

(1. Swinburne College, Shandong University of Science and Technology, Jinan, 250031, Shandong Province, China;）

Yunfang Lv（Corresponding author, Email:19051697635@163.com）

Abstract

High-frequency flapping-wing mechanisms have attracted increasing interest in micro aerial vehicles and low-altitude intelligent systems because of their strong hovering performance, high maneuverability, and adaptability to complex environments. However, most existing dynamic studies assume ideal kinematic joints and rigid components, limiting their ability to capture the coupled effects of revolute-joint clearances, structural flexibility, and wear. In this study, a rigid–flexible coupled dynamic model is developed for a high-frequency flapping-wing mechanism considering revolute-joint clearances and wear evolution. Contact–impact and frictional effects at the clearance joints are incorporated, while the flexible wing components are modeled using the absolute nodal coordinate formulation (ANCF). An Archard-based wear model is further introduced to describe clearance-induced degradation. The effects of component flexibility, clearance size, number of clearance joints, and flapping frequency on the dynamic response and wear behavior of the mechanism are systematically investigated. The results show that larger clearances, a greater number of clearance joints, and higher flapping frequencies intensify response fluctuations and increase the peak acceleration, driving torque, and contact–impact force. Structural flexibility further modifies the contact behavior through elastic deformation and energy transfer, thereby amplifying impact responses during certain phases of motion. The proposed framework provides a theoretical basis for dynamic performance assessment, wear prediction, and reliability-oriented design of high-precision biomimetic flapping-wing mechanisms.

Keywords: high-frequency flapping-wing mechanism; revolute joint clearance; rigid–flexible coupling; dynamic response; wear characteristics

1. Introduction

High-frequency flapping-wing mechanisms are key components of miniature biomimetic aerial vehicles and have attracted considerable attention because of their potential for highly maneuverable and agile flight. By exploiting aerodynamic and biomechanical principles, these mechanisms can provide efficient hovering, low observability, and a wide flight envelope, making them promising for a variety of miniature aerial platforms. Most existing dynamic analyses, however, assume ideal kinematic joints and rigid components. In practical mechanisms, revolute-joint clearances are unavoidable because of manufacturing tolerances and limitations in assembly accuracy. During high-frequency reciprocating motion, these clearances allow additional relative motion between the shaft and bushing, resulting in repeated impacts, vibration, and discontinuous load transmission. Such effects can accelerate joint wear, degrade motion accuracy, and reduce the reliability of the aerodynamic output. In addition, deformation of the main flapping wing can alter load transmission and further complicate the system dynamics. Therefore, the combined effects of joint clearance, structural flexibility, and wear must be considered to accurately characterize the dynamic behavior and service performance of high-frequency flapping-wing mechanisms.

In recent years, extensive research has been conducted on the dynamic responses of mechanisms with joint clearances and component flexibility. For example, Song et al. [1] developed a rigid–flexible model for a 4-4R mechanism and introduced a stepwise strategy for identifying dynamic parameters and compensating for nonlinear friction. The influence of external loading on flexible deformation was examined by Guo et al. [2] using a hub–beam–tip-mass system, showing that both the magnitude and direction of loading can significantly affect the response of a flexible component. Xiao et al. [3] extended rigid–flexible modeling to a multilink mechanism with irregular wear-induced clearances and demonstrated experimentally that clearance size and driving speed can modify not only the response amplitude but also bifurcation and chaotic behavior. Similar rigid–flexible concepts have also been applied outside conventional linkage systems; Sun et al. [4] studied the dynamic response and progressive collapse of a cable-net structure containing both rigid and flexible boundaries .The role of joint clearance becomes particularly important when flexibility is incorporated into the transmission chain. Wei et al. [5] investigated a cam–four-bar mechanism with

multiple clearances and showed that rotational speed, material properties, and joint clearance jointly influence motion accuracy. Lubrication was introduced into a rigid–flexible six-link mechanism by Li et al. [6], who examined how lubrication conditions and clearance parameters affect nonlinear dynamic behavior . Using the absolute nodal coordinate formulation, Wang et al. [7] modeled a spatial slider–crank mechanism and quantified the effects of component flexibility and elastic modulus on motion accuracy and joint reactions . Rigid–flexible coupling has also been used to describe large engineering systems, as demonstrated by Li et al. [8] in their dynamic model of a riser–LMRP/BOPs–wellhead system . Zhang et al. [9] applied a rigid–flexible formulation to a hydraulic six-degree-of-freedom parallel mechanism and identified the contribution of sealing elements to the flexible modes of the system. Other studies have focused more directly on how structural compliance changes the dynamic characteristics of mechanisms. Lobontiu et al. [10] formulated a dynamic compliance model for a planar parallelogram mechanism containing flexure hinges and examined the dependence of its natural frequencies on geometric parameters. Lai et al. [11] investigated the nonlinear vibration of a flexible tube subjected to cross-flow and showed that variations in squeeze-film thickness can change the stability and bifurcation characteristics of the system. Zheng et al. [12] combined a pseudo-rigid-body description with model-order reduction to improve the computational efficiency of dynamic analysis for a hybrid compliant mechanism.The interaction between flexibility and clearance has subsequently received increasing attention. Niu et al. [13] incorporated lubricated revolute and translational clearance joints into a rigid–flexible model and found that lubrication can suppress response peaks and reduce nonlinear instability. Li et al. [14] compared harmonic excitation and connecting-rod flexibility in a slider–crank mechanism with clearance and showed that the two factors affect both dynamic response and wear in different ways . Hou et al. [15] treated the socket of a spherical clearance joint as a flexible component and demonstrated that local compliance can mitigate part of the clearance-induced dynamic response. Xin et al. [16] coupled three-dimensional revolute clearance, structural flexibility, and the Archard wear formulation to investigate dynamic response, reliability, and wear evolution in a hybrid mechanism. At another scale, Yi et al. [17] developed a macro–micro coupled framework for a thin-walled spiral bevel gear transmission and showed that structural compliance and evolving contact conditions can strongly influence nonlinear contact behavior. Jia et al.[18]developed a Morris-based model reduction method for a 5-DOF hybrid robot with joint clearance and structural flexibility, reducing computational cost by 40% while preserving displacement and velocity accuracy. Ali et al.[19] incorporated crosspiece inertia and frictional impacts into a universal joint model with radial clearance to investigate nonlinear responses, including quasi-periodic oscillations, grazing bifurcations, and chaos.

However, frequent impacts and stress concentrations caused by clearances inevitably lead to wear-induced degradation of joint surfaces, which in turn alters the system's dynamic characteristics. Consequently, the wear characteristics and evolution of joints in mechanisms with clearances and rigid–flexible coupled mechanisms have attracted considerable research attention in recent years. Dou et al. [20] considered coupled bearing clearances and lubrication in a diesel-engine connecting-rod system and related wear-induced clearance evolution to changes in contact force and lubrication conditions . Zhao et al. [21]combined the absolute nodal coordinate formulation with the Archard model to calculate wear in revolute clearance joints of flexible multibody systems and demonstrated the importance of both structural flexibility and clearance size. From a vibration perspective, Ebrahimi et al. [22] showed that joint stiffness associated with clearance contact can significantly alter the instantaneous natural frequencies and mode shapes of flexible mechanisms.Lubricated clearance joints introduce an additional coupling between impact mechanics and tribological behavior. Wang et al. [23] investigated small-end-bearing wear in a crank–connecting rod–piston mechanism and showed that the evolving wear profile affects both impact behavior and lubrication performance. Lu et al. [24] modeled irregular wear clearances in a rigid–flexible steering actuator and demonstrated that wear evolution can substantially modify its phase trajectories and nonlinear characteristics. Instead of predicting wear alone, Wang et al. [25] combined finite-element analysis with multiobjective optimization to reduce contact forces and stresses in a clearance-containing slider–crank mechanism . Under heavy-load conditions, Lu et al. [26] showed that oil-film deterioration can intensify clearance-induced impacts and accelerate wear in a pushrod mechanism.Structural compliance has also been explored as a means of modifying clearance-induced contact. Erkaya et al. [27] compared conventional and partly compliant slider–crank mechanisms and found that flexure hinges can suppress impact and help maintain continuous joint

contact. Hu et al. [28] investigated fretting wear in flexible thin-walled bearings and identified different wear regimes associated with rolling and sliding contact during long-term operation. Song et al. [29] developed a nonsmooth rigid–flexible multibody formulation capable of accounting for different clearance types and lubrication conditions, allowing the influence of contact parameters and material properties to be evaluated systematically. Zhang et al. [30] investigated friction effects in a variable stator vane mechanism with clearance joints, identifying the Brown–McPhee model as the most stable and efficient among five friction models and revealing a nonmonotonic relationship between friction coefficient and system stability. Li et al. [31] combined contact-surface discretization, the LuGre friction model, and the Archard formulation to describe spatially nonuniform wear in mechanisms containing multiple clearances.Additional studies have demonstrated that clearance wear is sensitive to factors beyond nominal clearance size. Wang et al. [32] showed that crankshaft misalignment can modify bearing frictional loss and volumetric wear in a system with multiple lubricated clearances. Tang et al. [33] addressed frictional sliding contact between a flexible beam and a rigid hole and developed a contact formulation suitable for large relative sliding. Yin et al. [34] investigated the simultaneous effects of hinge clearance and joint-axis deviation in a landing-gear mechanism and showed that the two geometric imperfections interact in determining the transmitted load. Liu et al. [35] established a coupled tribo-dynamic formulation in which structural deformation and lubricant-film pressure are solved within the same clearance-joint framework.Contact characteristics have also been evaluated using alternative quantitative measures. Chen et al. [36] introduced an entropy-based index for evaluating the nonlinear characteristics of clearance-joint contact forces and examined its dependence on angular velocity and clearance size. Su et al. [37] incorporated cage flexibility and transient impact into the dynamic analysis of a four-point contact ball bearing and related these effects to skidding, whirl, and pocket wear. Questa et al. [38] further demonstrated that lubrication, flexibility, and roller-contact dynamics need to be considered together when predicting wear in high-speed rolling-element bearing systems.Collectively, these investigations confirm that joint wear is controlled by the combined effects of contact load, relative sliding, structural compliance, lubrication, and evolving geometry. Nevertheless, their conclusions cannot be transferred directly to a high-frequency flapping-wing mechanism, where repeated motion reversal produces strongly phase-dependent impact events and where deformation of the main wing can modify load transmission throughout the linkage.

The preceding literature review identifies several gaps in existing research on high-frequency flapping-wing mechanisms. First, although clearance-induced dynamic responses and wear have been extensively investigated, most studies focus on conventional mechanisms and general rigid–flexible coupled systems. Limited attention has been paid to the coupling among high-frequency reciprocating motion, flexible deformation, and joint clearances in high-frequency flapping-wing mechanisms. Consequently, the effects of clearance-induced nonlinearities on their dynamic performance and long-term service behavior remain insufficiently explored. Second, the effects of main-wing flexibility on clearance-induced impacts and joint wear in high-frequency flapping-wing mechanisms remain insufficiently understood. In particular, further analysis is needed to determine how main-wing deformation alters contact loads and wear distributions at revolute joints with clearance.Third, existing studies on clearance-induced wear primarily examine contact parameters, clearance size, friction coefficient, and accumulated sliding distance. In high-frequency flapping-wing mechanisms, however, main-wing flexibility may interact with clearance size, the number and locations of clearance joints, and drive speed to affect joint contact behavior and wear. Their combined effects on shaft–bearing contact loads, impact characteristics, and wear evolution have yet to be fully elucidated.

To address these gaps, this study makes the following contributions:

(1) A dynamic analysis framework incorporating multiple coupled factors is developed for high-frequency flapping-wing mechanisms. Revolute joint clearances, flexible deformation, and wear evolution are incorporated into a unified dynamic model, enabling coupled clearance–flexibility–wear analysis.

(2) A flexible modeling approach based on the absolute nodal coordinate formulation (ANCF) is introduced to capture the deformation characteristics of the flexible main-wing region. The effects of this flexible region on clearance-induced impact loads and joint wear distributions are investigated.

(3) The interaction mechanisms between flexible components and revolute joint clearances are elucidated, and the conditions under which flexibility amplifies or mitigates impact loads and wear

evolution are examined.

2. Formulation of the Joint Clearance Model

In this study, joint clearance, contact force, friction, wear, and absolute nodal coordinate formulation (ANCF)-based flexible-body models are adopted as established modeling tools rather than presented as standalone theoretical contributions. These models are integrated into a coupled clearance–flexibility–wear analysis framework for high-frequency flapping-wing mechanisms. Accordingly, the modeling section focuses on how the constituent models are coupled through key variables, including impact forces, flexible-body deformation, and wear depth, rather than repeating derivations of established theories.

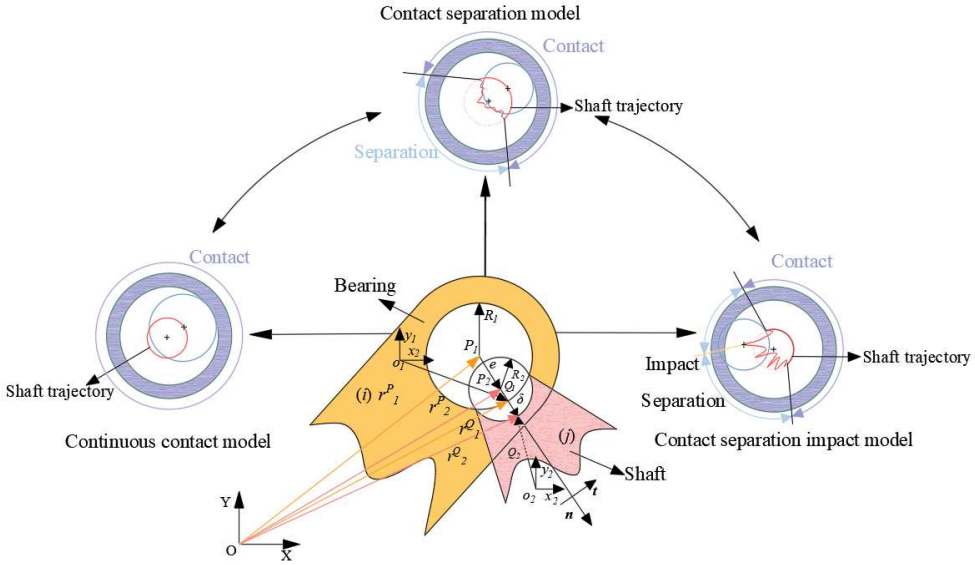


Fig.1. Relative configuration and vector definitions of a clearance joint.

2.1. Formulation of the Revolute Joint Clearance Model

Sustained reciprocating operation in flapping-wing mechanisms places continuous demands on the revolute joints responsible for motion and load transfer. Because manufacturing tolerances and assembly precision cannot be made arbitrarily small, a finite clearance between shaft and bushing is unavoidable in practice, which means the revolute constraint can no longer be treated as ideal. As the flapping frequency increases, relative motion within the clearance becomes more pronounced, potentially giving rise to repeated collisions, transient impacts, and frictional wear. These effects can alter the mechanism's motion accuracy, load transmission characteristics, and dynamic stability. Accordingly, the shaft and bushing are modeled as separate bodies, and a dynamic model of the clearance joint is formulated based on their relative displacement. This model provides a basis for elucidating the influence of joint clearance on the overall dynamic response under high-frequency operating conditions and for guiding structural refinement and performance improvement.

As shown in Fig. 1, the bushing and shaft centers are denoted by P_1 and P_2, respectively. To describe their relative motion, a global coordinate system O-XY is established, together with local coordinate systems o_1-x_1y_1 and o_2-x_2y_2 attached to the bushing and shaft, respectively. The positions of P_1 and P_2 are expressed by their respective position vectors $\boldsymbol{r}_1^0$ and $\boldsymbol{r}_2^0$ in the global coordinate system.

The relative position of the shaft center with respect to the bushing center is described by the eccentricity vector, defined as follows:

$$\boldsymbol{e} = \boldsymbol{r}_2^0 - \boldsymbol{r}_1^0 \tag{1}$$

where $\boldsymbol{r}_1^0$ and $\boldsymbol{r}_2^0$ denote the position vectors of the bushing center and the shaft center in the global coordinate system, respectively. The magnitude of the eccentricity vector is defined as the eccentricity and can be expressed as follows:

$$e = \sqrt{\boldsymbol{e}^{\mathrm{T}}\boldsymbol{e}} \tag{2}$$

For a planar revolute joint, the positions of the bushing center and the shaft center can be written,

respectively, as follows:

$$\boldsymbol{r}_1^0 = \left[x_1, y_1\right]^{\mathrm{T}} \qquad \boldsymbol{r}_2^0 = \left[x_2, y_2\right]^{\mathrm{T}} \tag{3}$$

Thus, the eccentricity vector can be further expressed as follows:

$$\boldsymbol{e} = \left[x_2 - x_1, y_2 - y_1\right]^{\mathrm{T}} \tag{4}$$

The corresponding eccentricity is given by:

$$\boldsymbol{e} = \sqrt{\left(x_2 - x_1\right)^2 + \left(y_2 - y_1\right)^2} \tag{5}$$

where e describes the magnitude and direction of the relative displacement between the bushing center and the shaft center, whereas $\boldsymbol{e}$ is the corresponding scalar distance and serves as a key parameter for determining the shaft–bushing contact state.

The radial clearance is given by $\boldsymbol{c} = \boldsymbol{R_1} - \boldsymbol{R_2}$. The eccentricity $\boldsymbol{e}$, corresponding to the magnitude of the eccentricity vector, satisfies $\boldsymbol{e} \geqslant 0$. Contact in the revolute joint with clearance is assessed using the penetration depth δ, calculated by subtracting the radial clearance from the eccentricity:

$$\delta = \left|\boldsymbol{r}_1^Q - \boldsymbol{r}_2^Q\right| = e - c \tag{6}$$

Here $\boldsymbol{c}$ is the radial clearance and $\boldsymbol{e}$ the eccentricity between the two centers. Note that δ carries a sign — it is not simply the length of the relative displacement vector, but a signed scalar used to classify the contact state of the shaft–bushing pair."

The presence of clearance in the revolute joint causes the relative motion between the shaft and bushing to evolve as their geometric constraints change. Based on their contact behavior during motion, the shaft–bushing interface can be classified into three distinct states: separation, sustained contact, and impact. The corresponding physical characteristics are illustrated in Fig. 1.

To further describe the contact behavior within the clearance revolute joint, criteria are established to identify the shaft–bushing interface state. The impact and separation states can be distinguished based on the relative positions of the two bodies and their contact deformation. These criteria are defined as follows:

$$\begin{cases} \delta > 0, & \text{Collision state} \\ \delta = 0, & \text{Continuous contact state} \\ \delta < 0, & \text{Non-contact state} \end{cases} \tag{7}$$

The position vectors of the contact points in the global coordinate system can be expressed as follows:

$$\boldsymbol{r}_j^Q = \boldsymbol{r}_j^0 + R_j \boldsymbol{n}_R \left(j = 1, 2\right) \tag{8}$$

When an instantaneous impact occurs between the shaft and bushing, the velocity vectors at the interface contact points can be expressed as follows:

$$\dot{\boldsymbol{r}}_j^Q = \dot{\boldsymbol{r}}_j^0 + R_j \dot{\boldsymbol{n}}_R \left(j = 1, 2\right) \tag{9}$$

where

$$\dot{n} = \frac{\dot{\boldsymbol{e}} e - \dot{e} \boldsymbol{e}}{e^2} \tag{10}$$

The normal and tangential components of the velocity of the bushing contact point relative to the shaft can be expressed, respectively, as follows:

$$\begin{bmatrix} v_n \\ v_{\mathrm{t}} \end{bmatrix} = \begin{bmatrix} \left(\dot{\boldsymbol{r}}_2^Q - \dot{\boldsymbol{r}}_1^Q\right)^{\mathrm{T}} & 0 \\ 0 & \left(\dot{\boldsymbol{r}}_2^Q - \dot{\boldsymbol{r}}_1^Q\right)^{\mathrm{T}} \end{bmatrix} \begin{bmatrix} \boldsymbol{n}_R \\ \boldsymbol{t}_R \end{bmatrix} \tag{11}$$

where $\boldsymbol{n}_R$ is the unit normal vector in the direction of the eccentricity vector, and $\boldsymbol{t}_R$ is the unit tangent vector obtained by rotating $\boldsymbol{n}_R$ counterclockwise by 90°.

2.2. Formulation of the Normal Contact Force Model

Normal impacts at the shaft–bushing interface are described here using the Lankarani–Nikravesh (L–N) contact formulation [39]. Its normal contact force combines two contributions: an elastic term governed by the penetration depth, and a velocity-dependent viscous damping term that

captures energy losses from local plastic deformation and internal material damping during the impact event.

According to the contact-state criteria established in Section 2.1, the normal contact force is calculated only when the shaft and bushing are in contact. When the penetration depth satisfies $\delta > 0$, the two contacting surfaces undergo compressive deformation, and the L–N model is used to calculate the normal impact force. When $\delta < 0$, the shaft and bushing are separated, with no normal contact interaction; hence, the normal contact force is zero. The corresponding normal impact force is expressed as follows:

$$F_n = K\delta_R^n + D\dot{\delta} \tag{12}$$

where n = 1.5, K represents the contact stiffness coefficient, and D is the damping coefficient. The penetration rate is denoted by $\dot{\delta}$. The coefficient K is calculated using the following expression:

$$K = \frac{4}{3\left(\sigma_1 + \sigma_2\right)}\left(\frac{R_1 R_2}{R_1 + R_2}\right)^{\frac{1}{2}} \tag{13}$$

where σ_1 and σ_2 denote the Poisson's ratios of the two contacting materials, respectively. The following sign convention is adopted for the curvature of the contact surfaces: positive for convex surfaces and negative for concave surfaces.

In Eq. (12), D can be expressed as follows:

$$D = \frac{3K(1-c_e{}^2)\delta_R^{\mathrm{n}}}{4\dot{\delta}^{(-)}} \tag{14}$$

where $\dot{\delta}^{(-)}$ denotes the initial impact velocity, and c_e is the coefficient of restitution.

2.3. Formulation of the Tangential Contact Force Model

Friction at the contact interface follows the modified Coulomb model of Ambrósio [40]. A key feature of this formulation is the correction coefficient cd, which smooths the otherwise abrupt sign change in friction force as the sliding velocity crosses zero — a discontinuity that would otherwise destabilize the numerical integration.The resulting friction force is expressed as follows:

$$F_t = -\mu_f c_d F_n \frac{v_t}{|v_t|} \tag{15}$$

where μ_f denotes the friction coefficient, and c_d denotes the dynamic correction coefficient, defined as follows:

$$c_d = \begin{cases} 0 & |v_t| < v_0 \\ \dfrac{|v_t| - v_0}{v_1 - v_0} & v_0 \le |v_t| \le v_1 \\ 1 & |v_t| > v_1 \end{cases} \tag{16}$$

where v_1 and v_0 denote the prescribed upper and lower velocity thresholds, respectively, and v_t denotes the relative tangential velocity.

3. Formulation of the Wear Model Accounting for Joint Clearance

The Archard wear law is adopted to predict adhesive wear at the clearance joints because of its simple formulation and its suitability for relating wear to contact load and relative sliding. Its mathematical expression is given by:

$$V = \frac{K_m F_n S}{H} \tag{17}$$

where V represents the volume of material removed by wear, and K_m is the wear coefficient. The cumulative sliding distance of an individual element is denoted by S, while F_n represents the normal impact force. The parameter H corresponds to the indentation hardness of the softer material

in the contact pair.

In engineering applications, the wear depth h generally provides a more intuitive measure of wear severity than the wear volume. Thus, dividing both sides of the equation by the actual contact area A allows the Archard wear model to be rewritten as follows:

$$h = K_d PS \tag{18}$$

where $K_d = \frac{K_m}{H}$ is the dimensional wear coefficient; $P = \frac{F_n}{A}$ denotes the contact pressure generated by the normal impact load acting over the actual contact area.

Since the contact force and relative sliding velocity in joints with clearance vary during operation, the Archard wear model can be expressed in differential form as follows:

$$dh = K_d P ds \tag{19}$$

where dh denotes the increment in wear depth, and ds denotes the relative sliding distance increment. Using $ds = vdt$, Eq. (19) can be further rewritten as follows:

$$dh = K_d P v dt \tag{20}$$

As the shaft and bushing undergo repeated contact and impact, the total wear depth is obtained by accumulating the local wear increments over successive sliding contact events:

$$h = \sum_{n=1}^{N} h_n \tag{21}$$

where h_n denotes the wear depth increment generated during the nth sliding contact event.

$$\begin{cases} R_1^* = R_1 + \dfrac{h}{2} \\ R_2^* = R_2 - \dfrac{h}{2} \end{cases} \tag{22}$$

where R_1^* and R_2^* denote the instantaneous equivalent radii of the bushing and shaft after wear, respectively.

Assuming identical material properties for the contacting surfaces of the shaft and bushing, the total wear is taken to be equally distributed between the two surfaces. Accordingly, the equivalent radii after wear can be expressed as follows:

4. Formulation of the Flexible Beam Element Model Based on the Absolute Nodal Coordinate Formulation (ANCF)

Capturing the in-plane deformation of the flexible wing requires a beam element formulation; a planar two-node ANCF element is therefore introduced to describe both the position and the deformation state of each flexible segment.

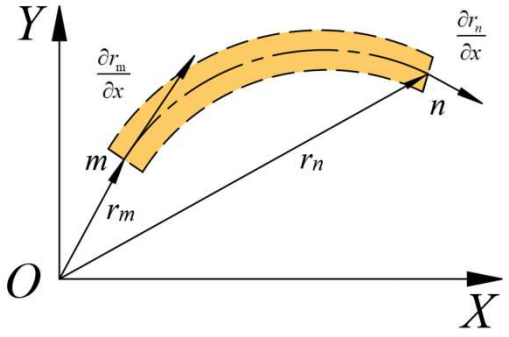


Fig.2. Planar flexible beam model

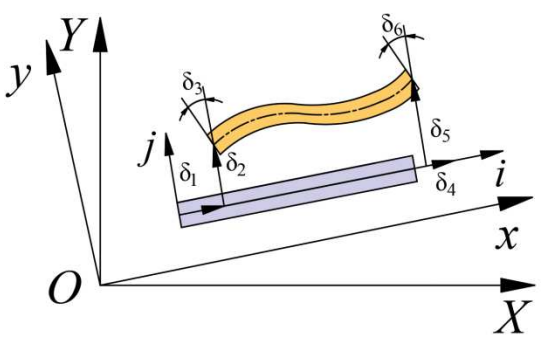


Fig.3. Geometric configuration of beam element

The two-dimensional, two-node beam element model is illustrated in Figs. 2 and 3, with O-XY denoting the inertial coordinate system. Position and gradient vectors are defined at nodes i and j to describe the deformation of the beam element. The vectors r_i and r_j denote the position vectors of the two nodes, respectively. The position vector of any point within the beam element can be obtained using interpolation functions as follows:

$$\boldsymbol{r}=\begin{bmatrix}X\\Y\end{bmatrix}=\begin{bmatrix}m_0+m_1x+m_2x^2+m_3x^3\\n_0+n_1x+n_2x^2+n_3x^3\end{bmatrix}=\boldsymbol{S}_{(x)}\boldsymbol{e}_{(t)} \tag{23}$$

where $m_i, n_i \ (i=0,1,2,3)$ are the interpolation coefficients, S is the beam element shape function matrix, and $\boldsymbol{e}$ is the nodal coordinate vector of the beam element.

The nodal coordinate vector $\boldsymbol{e}$ is expressed as follows:

$$\boldsymbol{e}=[\boldsymbol{r}_i^{\mathrm{T}}\ \boldsymbol{r}_{i,x}^{\mathrm{T}}\ \boldsymbol{r}_j^{\mathrm{T}}\ \boldsymbol{r}_{j,x}^{\mathrm{T}}]^{\mathrm{T}} \tag{24}$$

where each position vector has two components, and the vectors with subscripts x and y denote the gradient vectors at beam element nodes i and j in the corresponding directions. This yields:

$$\boldsymbol{e}=[r_{i1}, r_{i2}, \frac{\partial r_{i,1}}{\partial x}, \frac{\partial r_{i,2}}{\partial x}, r_{j1}, r_{j2}, \frac{\partial r_{j,1}}{\partial x}, \frac{\partial r_{j,2}}{\partial x}]^{\mathrm{T}} \tag{25}$$

The shape functions are defined as differentiable functions within the element. Four scalar shape functions are used to describe the two-dimensional, two-node beam element, and the corresponding shape function matrix is expressed as follows:

$$\boldsymbol{S}=[1-3\varsigma^2+2\varsigma^3,\ l\left(\varsigma-2\varsigma^2+\varsigma^3\right),\ 3\varsigma^2-2\varsigma^3,\ l\left(-\varsigma^2+\varsigma^3\right)]\otimes\boldsymbol{I}_2 \tag{26}$$

where $\varsigma=\frac{x}{l}$, l is the initial length of the beam element, $\otimes$ denotes the Kronecker product, and I_2 is the 2×2 identity matrix.

Time-differentiating the position field in Eq. (23) yields the velocity of an arbitrary material point on the element. Summing (integrating) these local kinetic energy contributions across the element length then gives the total kinetic energy expression below:

$$T_e=\frac{1}{2}\int_0^l \rho A\dot{\boldsymbol{r}}^{\mathrm{T}}\dot{\boldsymbol{r}}dx=\frac{1}{2}\int_0^l \rho A\dot{\boldsymbol{e}}^{\mathrm{T}}\boldsymbol{S}^{\mathrm{T}}\boldsymbol{S}\dot{\boldsymbol{e}}dx=\frac{1}{2}\dot{\boldsymbol{e}}^{\mathrm{T}}\boldsymbol{M}_e\dot{\boldsymbol{e}} \tag{27}$$

where ρ is the material density, A is the cross-sectional area, l is the initial length, and M_e is the mass matrix of the beam element. Since the shape function matrix S is independent of the nodal coordinates, the element mass matrix is constant and can be expressed as follows:

$$\boldsymbol{M}_e=\rho A\int_0^l \boldsymbol{S}^{\mathrm{T}}\boldsymbol{S}dx \tag{28}$$

For the two-dimensional, two-node beam element adopted in this study, the nodal coordinate vector $\boldsymbol{e}$ contains eight components. Accordingly, the mass matrix M_e is an 8×8 constant symmetric matrix.

During motion, the flexible beam element primarily undergoes axial stretching and bending. For an isotropic material, the elastic strain energy associated with axial deformation can be expressed as follows:

$$U_a=\frac{1}{2}\int_0^l \boldsymbol{E}\boldsymbol{A}\varepsilon_l^2 dx \tag{29}$$

where E is the Young's modulus of the beam material, A is the cross-sectional area, l is the initial element length, and ε_l is the axial strain. Based on the relationship between the elastic strain energy and the nodal coordinates, the elastic force arising from axial deformation can be expressed as follows:

According to the principle of virtual work, the generalized axial elastic force is obtained by differentiating the strain energy with respect to the nodal coordinate vector:

$$F_l=\frac{\partial U_a}{\partial e}=\int_0^l EA\varepsilon_l S_l \mathrm{d}x \tag{30}$$

where $S_l=S'^{\mathrm{T}}S'$.

For a two-dimensional, two-node beam element, the axial strain can be described by the change in distance between its two end nodes:

$$\varepsilon_a=\frac{l_e-l_0}{l_0} \tag{31}$$

where $l_e = \sqrt{\left(x_j - x_i\right)^2 + \left(y_j - y_i\right)^2}$ denotes the deformed length of the beam element, and l_0 denotes its initial length.

For a uniform flexible beam element with constant Young's modulus and cross-sectional area, the axial stiffness is expressed as follows:

$$K_l = \int_0^l EA\varepsilon_l S_l dx \tag{32}$$

In addition to axial extension and compression, the flexible beam element undergoes elastic deformation due to bending of its centerline. The elastic strain energy associated with bending can therefore be expressed as follows:

$$U_b = \frac{1}{2}\int_0^l \boldsymbol{EI}\kappa^2 dx \tag{33}$$

where I is the second moment of area of the beam cross-section, κ is the curvature of the beam centerline, and E is the Young's modulus of the material.

For small deformations of the beam element, the elastic bending force is given by:

$$F_t = \frac{\partial U_b}{\partial e} = \left(\int_0^l EIS''(S''^{\mathrm{T}})\ dx\right)e \tag{34}$$

For a uniform flexible beam element with constant Young's modulus and second moment of area, the bending stiffness is expressed as follows:

$$K_t = \int_0^l EIS''(S''^{\mathrm{T}})\ dx \tag{35}$$

The elastic force of the flexible beam element is the vector sum of the axial and bending elastic forces and can be expressed as follows:

$$F_e = F_l + F_t = K_l e + K_t e \tag{36}$$

5. Formulation of the Dynamic Model of a High-Frequency Flapping-Wing Mechanism with Revolute Joint Clearance

This study considers a bioinspired flapping-wing mechanism, simplified as a planar multibody system to capture its primary flapping motion within the plane of motion. Given the high structural symmetry of the mechanism, only one side is modeled to improve the efficiency of multibody dynamic modeling and numerical solution. The equivalent planar model consists primarily of rigid links, flexible main-wing components, and revolute joints with clearance. The driving force acts on the input link and is transmitted through the multilink transmission system to the distal wing components, producing periodic flapping motion. The model is used to investigate the effects of revolute joint clearance and main-wing flexibility on the dynamic response, motion stability, and wear characteristics of the mechanism.

The main components of the flapping-wing mechanism are shown in Fig. 6. The transmission links primarily transmit power and provide structural support and are therefore modeled as rigid bodies. Key main-wing components that undergo elastic deformation are modeled as flexible bodies to capture their deformation during high-speed flapping. The flexible main wing stores and releases elastic energy during motion, thereby altering joint contact conditions and transient loads.

For the dynamic analysis, carbon fiber is assigned to all mechanical components, including the rigid links, flexible main-wing components, transmission shafts, and bushings. The corresponding material properties are incorporated into both the contact-force calculations and the flexible-component models developed using the absolute nodal coordinate formulation (ANCF). Table 1 presents the structural parameters of the flapping-wing mechanism. The material properties, contact parameters, and simulation settings adopted in the analysis are provided in Table 2.



Fig.4. 3D rendering of the high-frequency Flapping-Wing Mechanism.

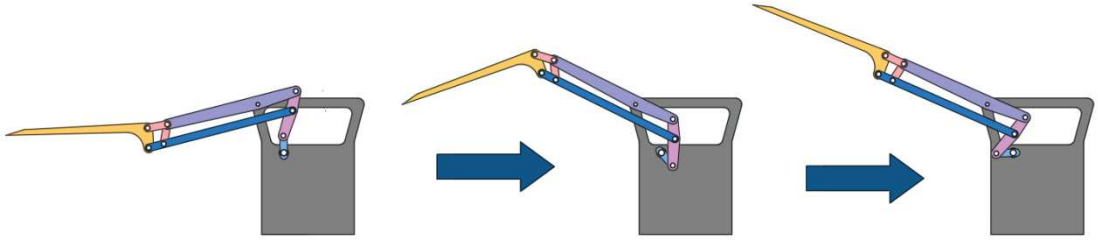


Fig.5. Motion process of the flapping wing

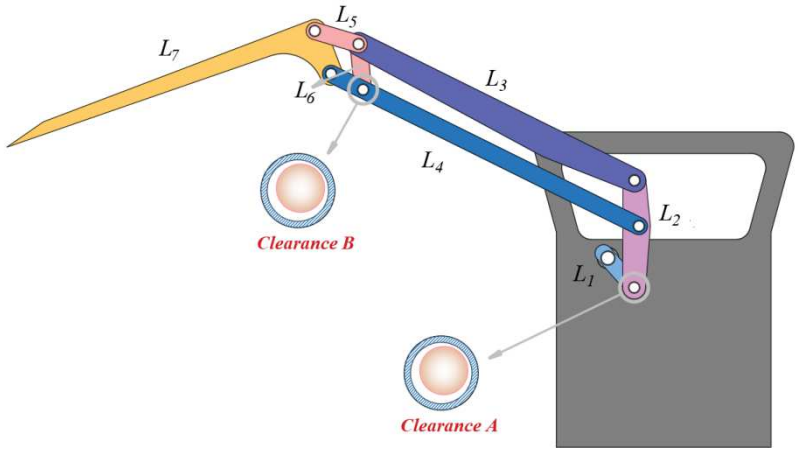


Fig.6. Schematic diagram of the left-side high-frequency Flapping-Wing Mechanism.

This study investigates a high-frequency flapping-wing mechanism, focusing on the dynamic characteristics of revolute joint A with clearance. Joint A is selected as a representative clearance joint because it is located within the drive linkage and directly accommodates relative motion between the shaft and bushing during operation. Consequently, impact, friction, and wear at this joint can significantly affect the mechanism's dynamic response, motion stability, and wear evolution. In addition, component L_7 is modeled as a flexible component representing the main wing. Introducing clearance into joint A enables a clearer investigation of the dynamic coupling between the flexible region and the clearance joint.

Although multiple components in an actual flapping-wing mechanism may undergo flexible deformation, L_7 is selected as the primary flexible region in the present model because the main-wing region has a relatively large mass, exhibits pronounced deformation, and directly influences aerodynamic force generation. The effects of flexibility in the remaining components will be investigated in future work.

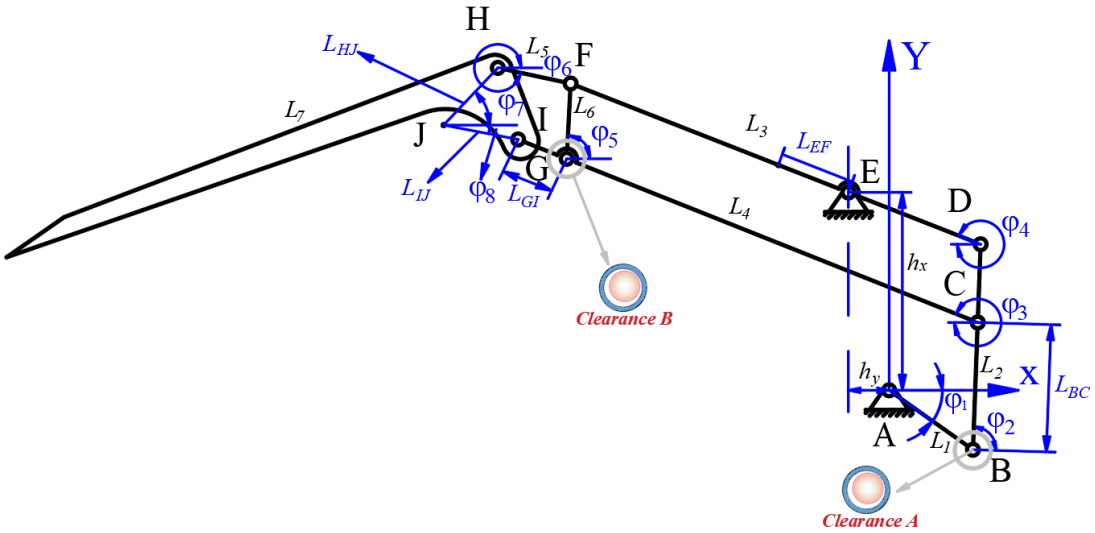


Fig.7. Kinematic diagram of the left-side high-frequency Flapping-Wing Mechanism

The rigid components are described using reference-point coordinates, with each rigid body having three independent generalized coordinates to characterize its planar motion. All components except the main-wing component L7 are treated as rigid bodies. Their generalized coordinates are expressed as follows:

$$q_{(i)} = \left(x_i \;\; y_i \;\; \theta_i\right)^{\mathrm{T}} \left(i = 1,2,3,4,5,6\right) \tag{37}$$

Component L_7 is modeled using the absolute nodal coordinate formulation (ANCF) and discretized into n elements, each with eight generalized coordinates. Its generalized coordinates are defined as follows:

$$q_{(7)} = \begin{Bmatrix} q^1_{(7)1} & q^1_{(7)2} & \cdots & q^1_{(7)8} \\ \vdots & \vdots & \vdots & \vdots \\ q^n_{(7)1} & q^n_{(7)2} & \cdots & q^n_{(7)8} \end{Bmatrix}^{\mathrm{T}} \tag{38}$$

The generalized coordinates of the system are defined as follows:

$$\boldsymbol{q} = \left(\boldsymbol{q}_{(1)} \;\; \boldsymbol{q}_{(2)} \;\; \boldsymbol{q}_{(3)} \;\; \boldsymbol{q}_{(4)} \;\; \boldsymbol{q}_{(5)} \;\; \boldsymbol{q}_{(6)} \;\; \boldsymbol{q}_{(7)}\right)^{\mathrm{T}} \tag{39}$$

The system constraint equations are expressed as follows:

$$\boldsymbol{\Phi}_{CF}\left(\boldsymbol{q}, t\right) = 0 \tag{40}$$

Differentiating the constraint equations in Eq. (40) once and twice with respect to time yields the velocity and acceleration constraint equations of the flapping-wing mechanism, respectively:

$$\boldsymbol{\Phi}_q \dot{\boldsymbol{q}} = -\boldsymbol{\Phi}_t \equiv \nu \tag{41}$$

$$\boldsymbol{\Phi}_q \ddot{\boldsymbol{q}} = -\left(\boldsymbol{\Phi}_q \dot{\boldsymbol{q}}\right)_q \dot{\boldsymbol{q}} - 2\boldsymbol{\Phi}_{qt}\dot{\boldsymbol{q}} - \boldsymbol{\Phi}_{tt} \equiv \boldsymbol{\gamma} \tag{42}$$

The Baumgarte constraint stabilization method is adopted, in which feedback terms associated with the position and velocity constraints are introduced into the system dynamic equations to dynamically correct constraint violations. Based on this method, the modified dynamic equations of the flexible flapping-wing mechanism with joint clearances are formulated as follows:

$$\begin{pmatrix} \boldsymbol{M} & \boldsymbol{\Phi}_{\mathrm{q}}^{\mathrm{T}} \\ \boldsymbol{\Phi}_{\mathrm{q}} & \boldsymbol{0} \end{pmatrix} \begin{pmatrix} \ddot{\boldsymbol{q}} \\ \boldsymbol{\lambda} \end{pmatrix} = \begin{pmatrix} Q \\ \boldsymbol{\gamma} - 2\alpha\dot{\boldsymbol{\Phi}} - \beta^2\boldsymbol{\Phi} \end{pmatrix} \tag{43}$$

where α and β are the Baumgarte stabilization parameters.

Table 1 Structural parameters of the High-Frequency Flapping-Wing Mechanism

Component	Length/mm	Mass/kg	Moment of inertia/10^{-3} kg·mm^2
Crank1	42.01	0.00221	Ixx=0.1983254472 Iyy=0.1863190926

Rod2	90.71	0.01151	Ixx =4.6796382024 Iyy =4.5075317518
Rod3	231.05	0.03128	Ixx =82.2473909747 Iyy =81.6645555874
Rod4	252.00	0.0573	Ixx =76.4868251036 Iyy =76.3436797294
Rod5	43.99	0.00384	Ixx =0.4094523317 Iyy =0.4001858709
Rod6	44.08	0.00334	Ixx =0.3142487099 Iyy =0.2913445509
Wing7	--	0.02456	Ixx =1222.6784533204 Iyy =2397.9268511806
L_{BC}	62.35	--	--
L_{EF}	26.98	--	--
L_{GI}	15.82	--	--
L_{HJ}	33.44	--	--

Table 2 Detailed simulation parameters

Parameter	Value	Parameter	Value
Bushing inner radius	3mm	*Wear coefficient(K_m)*	2.16×10^{-4}
Young's modulus of the material(E_k)	27.44GPa	*Linear wear coefficient(K_d)*	8×10^{-14}
Poisson's ratio of the material(v_k)	0.29	*Indentation hardness of the softer contact material (H)*	2.7×10^{9}

6. Effects of Component Flexibility on the Dynamic Response and Joint Wear Characteristics of a Rigid–Flexible Coupled High-Frequency Flapping-Wing Mechanism with Joint Clearances

6.1 Effects of Component Flexibility on the Dynamic Response of a Rigid–Flexible Coupled High-Frequency Flapping-Wing Mechanism with Joint Clearances

To investigate the influence of revolute joint clearance on the dynamic response of a high-frequency flapping-wing mechanism incorporating component flexibility, clearance A is selected as the representative clearance, and the flexibility of the main wing L_7 is considered. Following the study of a high-frequency flapping-wing mechanism by Zhou et al. [41], a drive speed of 450 rpm is adopted as a representative normal operating condition. The clearance is set to 0.3 mm. The mechanism is simulated over two operating cycles, and the main wing displacement, velocity, and acceleration, together with the driving torque and impact force at the clearance joint, are examined for both the fully rigid and flexible-component models, as shown in Figs. 8–12.

As shown in Figs. 8–12, joint clearance introduces pronounced local fluctuations in the dynamic response and increases the peak acceleration and driving torque. The displacement curves of the terminal main wing under the three conditions are generally similar, with deviations concentrated near the displacement extrema, as shown in Fig. 8. The minimum displacement of the rigid mechanism is slightly higher than that of the ideal mechanism, whereas that of the rigid–flexible coupled mechanism is slightly lower. This is mainly because clearance alters the effective kinematic constraints at the revolute joint, while elastic deformation is superimposed on the clearance-induced positional deviation, resulting in different deviations in the terminal displacement. As shown in Fig. 9, the rigid–flexible coupled mechanism exhibits more pronounced fluctuations near the velocity peaks, some of which exceed those of the rigid mechanism. This may result from impact-induced disturbances and the additional velocity contributed by elastic deformation. As shown in Fig. 10, both mechanisms with clearance exhibit pronounced acceleration spikes, while the rigid–flexible coupled mechanism displays more secondary fluctuations following the main

peaks. This is primarily because impacts cause rapid changes in component velocity over a short period and excite elastic vibrations in the flexible component, thereby intensifying the local acceleration response.

These effects are also reflected in the driving torque and impact force at the clearance joint. As shown in Fig. 11, the rigid–flexible coupled mechanism exhibits substantially higher peak driving torque and more local fluctuations than the rigid mechanism. This may be because impact loads transmitted to the drive are superimposed on elastic restoring forces and vibration-induced inertial loads, increasing the instantaneous torque required to maintain the prescribed motion. As shown in Fig. 12, the maximum impact force at clearance A increases considerably in the rigid–flexible coupled mechanism, whereas some secondary impact peaks are lower than those of the rigid mechanism. This indicates that the influence of flexibility on impacts varies with the phase of motion. A possible explanation is that elastic deformation alters the relative position and contact velocity between the bearing and shaft, while elastic recovery may either intensify or mitigate impacts at different stages. Thus, under the present operating conditions, component flexibility does not provide a consistent cushioning effect; instead, it increases the peaks of certain dynamic responses during some phases of motion.

Overall, under the present operating conditions, component flexibility has a limited influence on the overall displacement pattern of the terminal main wing but a more pronounced effect on local acceleration, driving torque, and impact force. This may be attributed to flexible deformation altering the relative motion and contact state at the clearance joint and affecting subsequent impacts through the storage and release of elastic energy. Therefore, component flexibility does not consistently cushion impacts under these conditions and instead increases impact loads during certain phases. The coupled effects of clearance-induced impacts and flexible vibration should therefore be considered in the dynamic analysis of the mechanism.

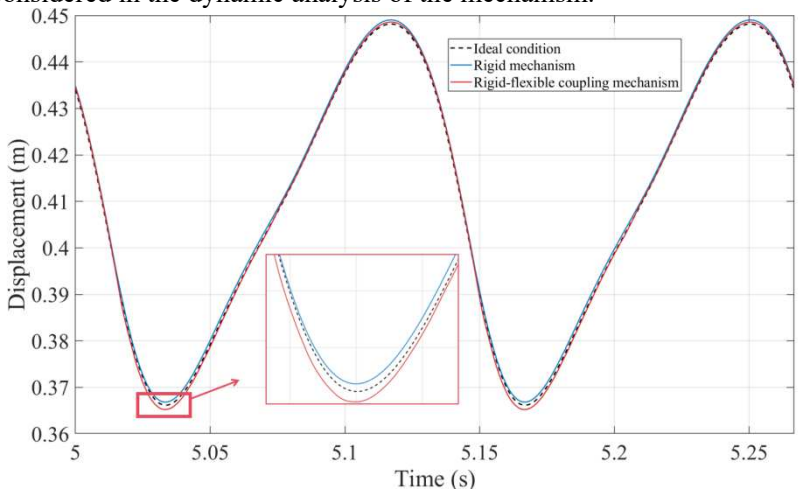


Fig.8. Displacement of the main wing

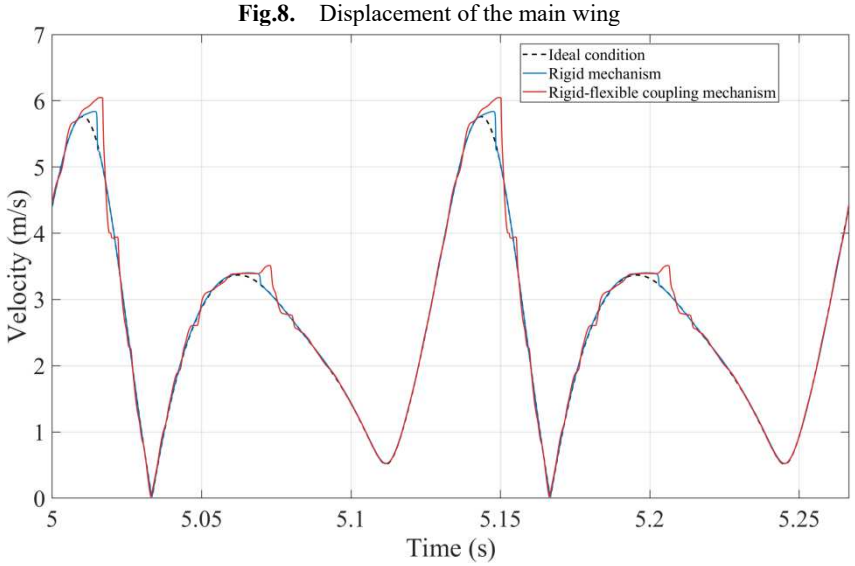


Fig.9. Velocity of the main wing

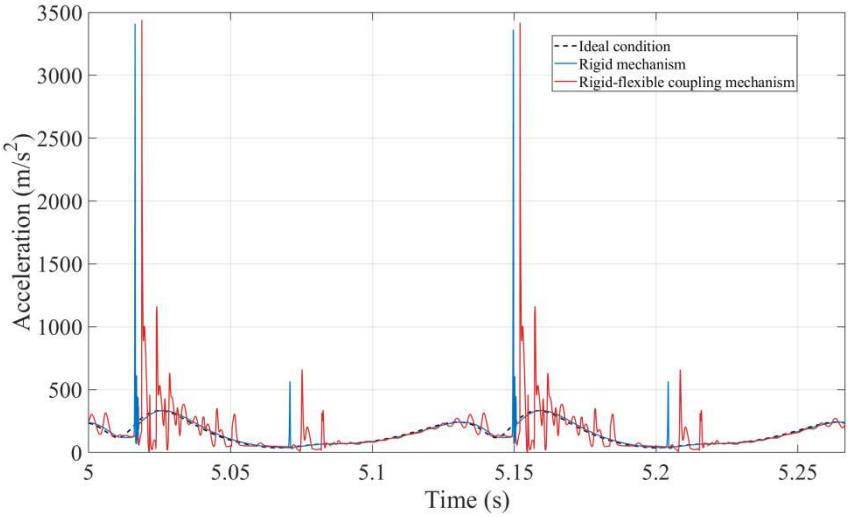


Fig.10. Acceleration of the main wing

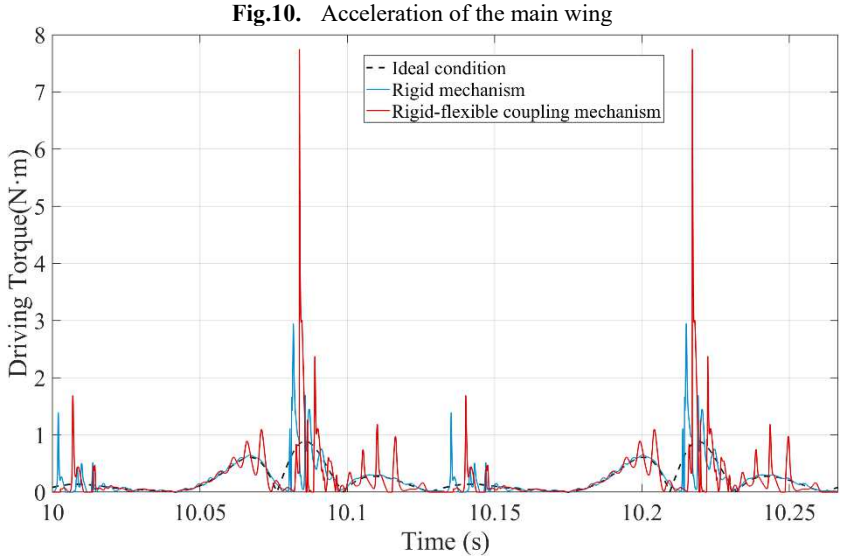


Fig.11. Driving Torque

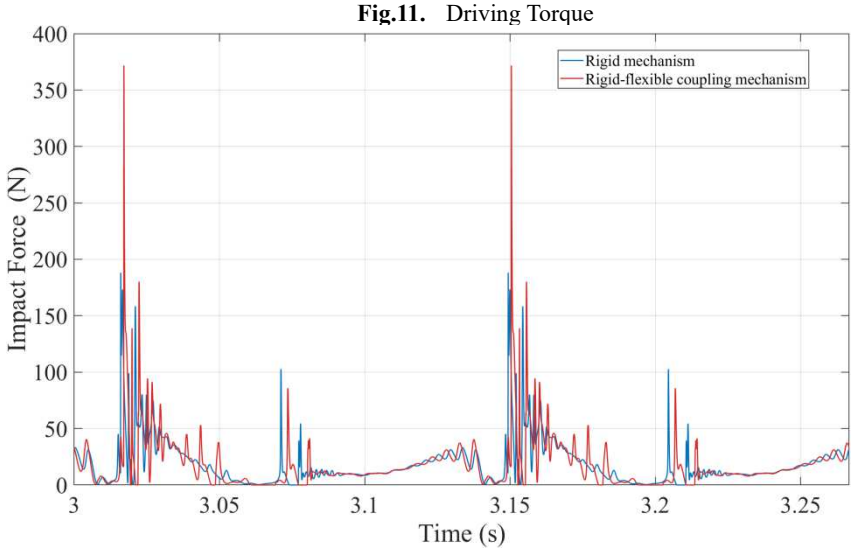


Fig.12. Impact force at clearance A

6.2 Effects of Component Flexibility on Revolute Joint Wear in a Rigid–Flexible Coupled High-Frequency Flapping-Wing Mechanism with Joint Clearances

To analyze the influence of component flexibility on the wear characteristics of revolute joints in a high-frequency flapping-wing mechanism, this section focuses on clearance A and compares the wear predicted by the rigid and rigid–flexible coupled models after 100 operating cycles at a

drive speed of 450 rpm and an initial clearance of 0.3 mm. In the calculations, the shaft and bushing surfaces are each uniformly discretized into 1,000 regions, and wear is accumulated at each location to obtain its distribution along the surfaces. Figure 13 presents the wear depth at clearance A, Fig. 14 shows the worn shaft profile and its local details, and Fig. 15 illustrates the center trajectories at clearance A for the two models, enabling local wear differences to be analyzed in relation to their relative motion.

As shown in Figs. 13 and 14, both the rigid and rigid–flexible coupled mechanisms exhibit pronounced circumferential nonuniformity in wear at clearance A, with greater wear concentrated primarily in the angular range of [210°,240°]. Compared with the rigid mechanism, the rigid–flexible coupled mechanism exhibits a more pronounced wear peak at approximately 220°, with a maximum wear depth of approximately 4.2×10^{-4} m, twice that of the rigid mechanism, which is approximately 2.1×10^{-4} m. In addition, appreciable wear occurs around 10°–30° in the rigid–flexible coupled mechanism, whereas wear in this region is relatively small in the rigid mechanism. As shown in Fig. 14, the shaft surfaces of both mechanisms remain close to the ideal profile over most angular positions, but pronounced material loss occurs in localized regions of concentrated wear. The rigid–flexible coupled mechanism exhibits a deeper profile depression at approximately 220°, corresponding to the wear peak in Fig. 13. This may be because elastic deformation alters the contact locations and load distribution between the shaft and bushing, exposing certain regions to higher contact pressures or greater cumulative relative sliding and thereby producing more concentrated local wear. Specifically, before an impact occurs, the flexible main wing deforms elastically under inertial loads, storing elastic energy in the structure. As the shaft approaches contact with the bearing, the recovery motion of the flexible component may further increase the relative velocity at initial contact, thereby increasing the peak normal impact force. During some phases of motion, however, flexible deformation can reduce abrupt changes in the relative velocity between components, resulting in a smoother contact process and providing some impact mitigation. Thus, flexibility does not simply produce a cushioning effect; instead, it can either intensify or mitigate clearance-induced impacts by altering the energy transfer pathways and contact dynamics of the system.

As shown in Fig. 15, the overall shapes of the center trajectories are similar for the two mechanisms. However, both exhibit repeated back-and-forth motion that deviates from the circumferential contour in the lower-left region, which approximately corresponds to the primary wear region. The rigid mechanism exhibits more pronounced trajectory crossings in this region, whereas the trajectories of the rigid–flexible coupled mechanism are more concentrated, with additional local deviations in the upper and upper-right regions. These differences indicate that flexibility alters the relative motion path and contact process. A greater degree of trajectory crossing does not necessarily imply a greater wear depth. Although the trajectories of the rigid–flexible coupled mechanism are more concentrated in the lower-left region, repeated contact may be confined to a narrower surface region. Combined with local load variations induced by elastic deformation, this can produce a deeper wear peak. Therefore, under the present operating conditions, component flexibility primarily redistributes contact locations and wear, while exacerbating wear in certain regions. The motion trajectories of the shaft and bearing, local contact loads, and relative sliding should therefore be considered together when evaluating joint wear and service life.

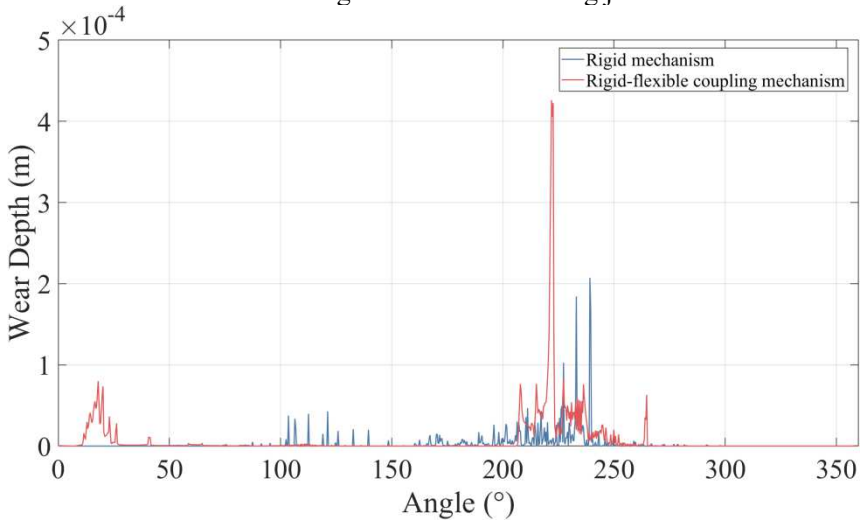
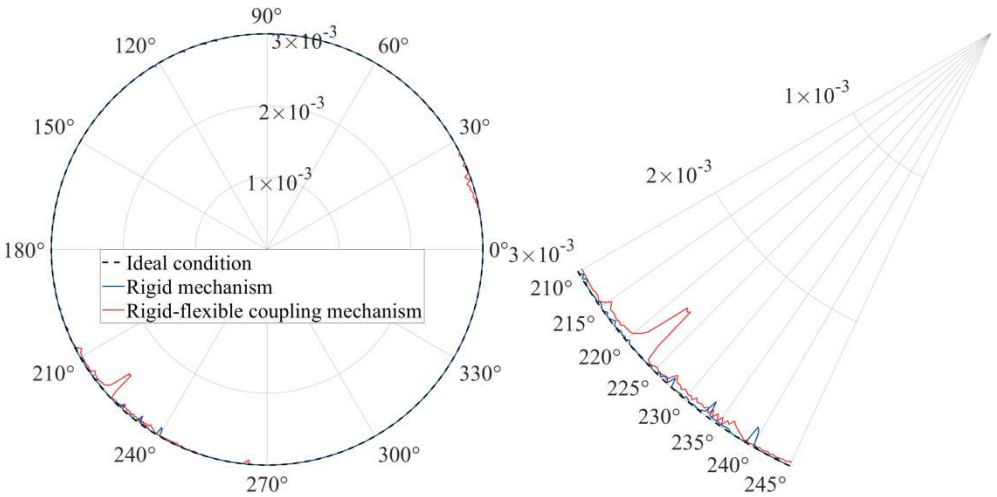


Fig.13. Wear depth at clearance A



(a) Worn surface of the shaft **(b)** Enlarged detail

Fig.14. Schematic diagram of shaft wear.

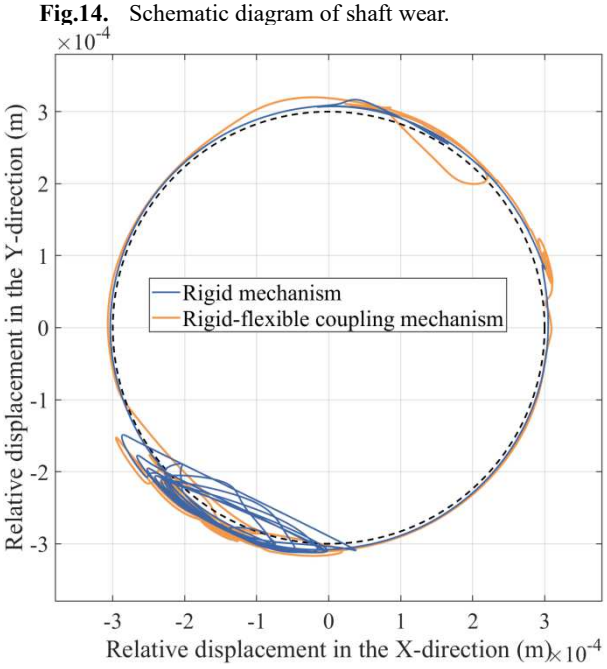


Fig.15. Center trajectory at clearance A

7. Effects of Drive Speed on the Dynamic Response and Wear Behavior of a Rigid–Flexible Coupled High-Frequency Flapping-Wing Mechanism with Joint Clearances

7.1 Effects of Drive Speed on the Dynamic Response of a Rigid–Flexible Coupled High-Frequency Flapping-Wing Mechanism with Joint Clearances

To investigate the influence of input rotational speed on the dynamic response of the rigid–flexible coupled high-frequency flapping-wing mechanism, three drive speeds—150, 300, and 450 rpm—are compared while the revolute joint clearance is maintained at 0.3 mm. Component L_1 is selected as the driving link and prescribed a constant angular velocity. The dynamic responses of the mechanism during the 18th and 19th operating cycles are shown in Figs. 16–20.

The displacement curves at different drive speeds largely overlap, exhibiting consistent peaks, troughs, and periodic patterns. This indicates that the input rotational speed does not significantly alter the overall motion trajectory of the main wing. However, as shown in Figs. 16 and 17, local differences near the displacement minima increase with rotational speed, indicating greater

susceptibility to clearance-induced disturbances near motion reversal. The velocity response is more sensitive to rotational speed, with its maximum increasing from approximately 2.2 m/s at 150 rpm to 4.1 m/s at 300 rpm and 6.0 m/s at 450 rpm. More pronounced abrupt drops and local fluctuations also occur during transitions between motion states.

As shown in Figs. 18–20, the acceleration, driving torque, and impact force exhibit increasingly pronounced transient impact characteristics as rotational speed increases. At 450 rpm, the acceleration curve displays pronounced peaks and closely spaced high-frequency pulses, reflecting repeated contact, separation, and recontact between the shaft and bushing. The maximum driving torques at 150, 300, and 450 rpm are approximately 1.5, 4, and 7.8N·m, respectively, while the corresponding maximum impact forces are approximately 55, 180, and 370 N. The approximately coincident peaks in acceleration, driving torque, and impact force indicate that transient loads generated by clearance-induced impacts are transmitted along the kinematic chain to the drive, producing simultaneous changes in the inertial response and driving load.

Overall, the input rotational speed primarily affects the amplitudes and fluctuation intensities of the dynamic responses, while its influence on the basic motion trajectory of the main wing is relatively limited. As rotational speed increases, transitions between contact states of the shaft and bushing become more rapid, and both impact intensity and the number of repeated impacts increase. Consequently, velocity fluctuations, acceleration peaks, and drive loads increase substantially. The drive speed should therefore be selected appropriately to meet the required flapping frequency and motion output. In addition, optimizing the clearance size, improving the cushioning characteristics of the contact region, and adjusting the drive control parameters can help reduce the transmission and accumulation of impact loads within the mechanism at high speeds.

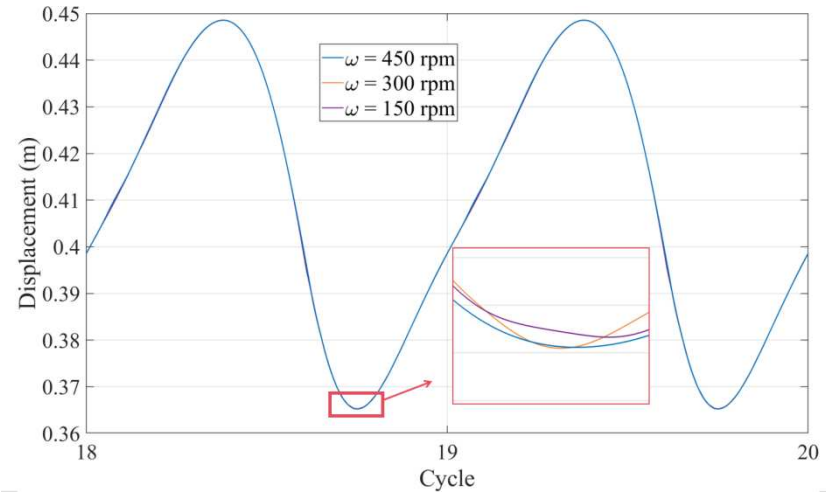


Fig.16. Displacement of the main wing

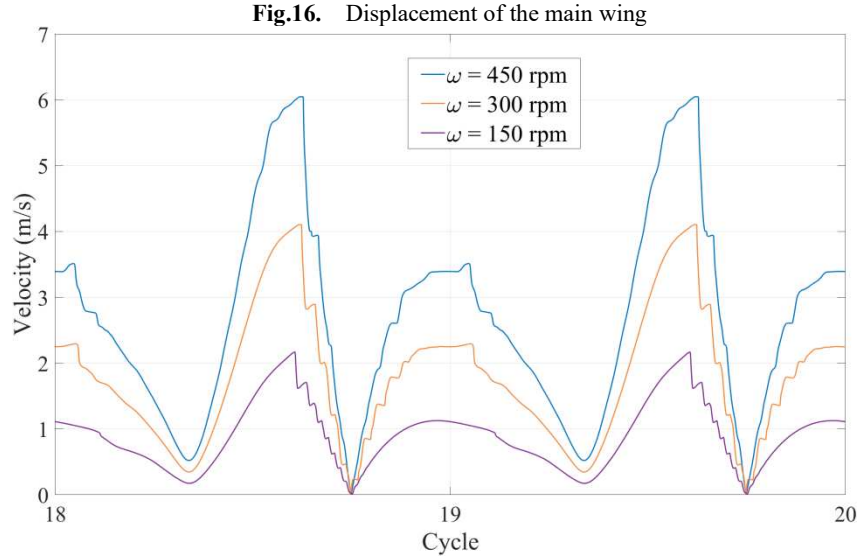


Fig.17. Velocity of the main wing

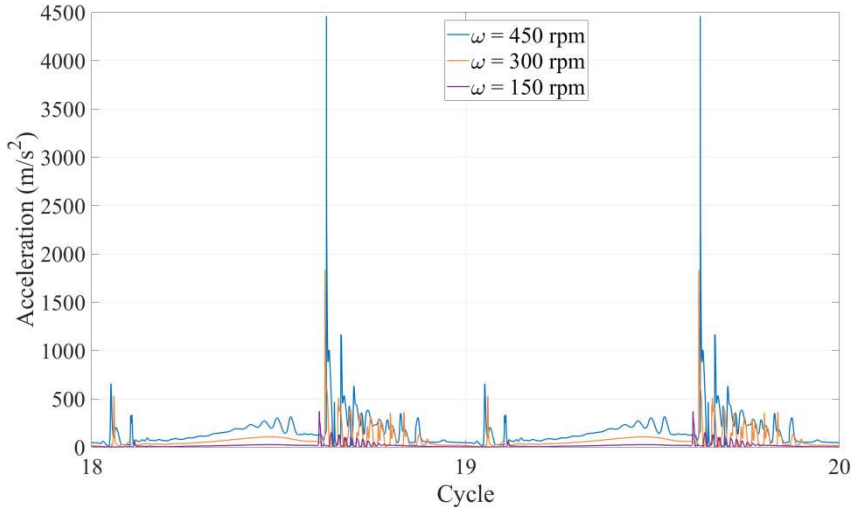


Fig.18. Acceleration of the main wing

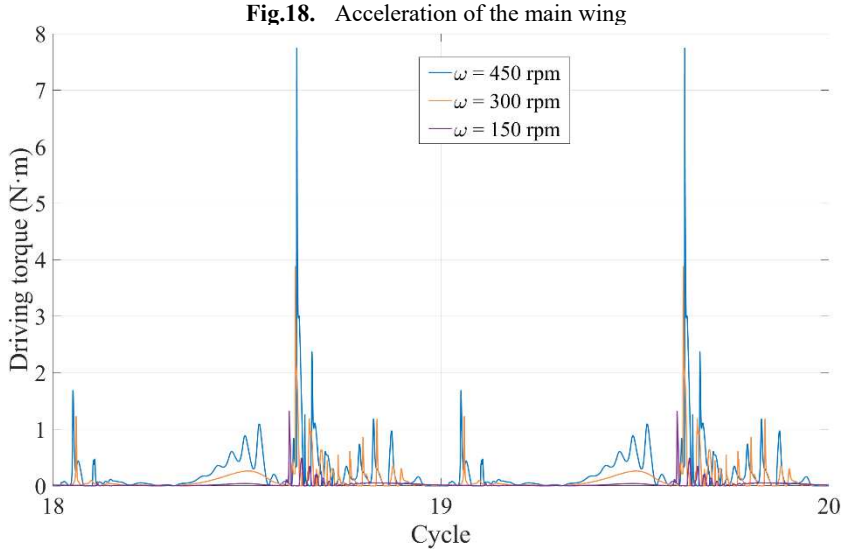


Fig.19. Driving Torque

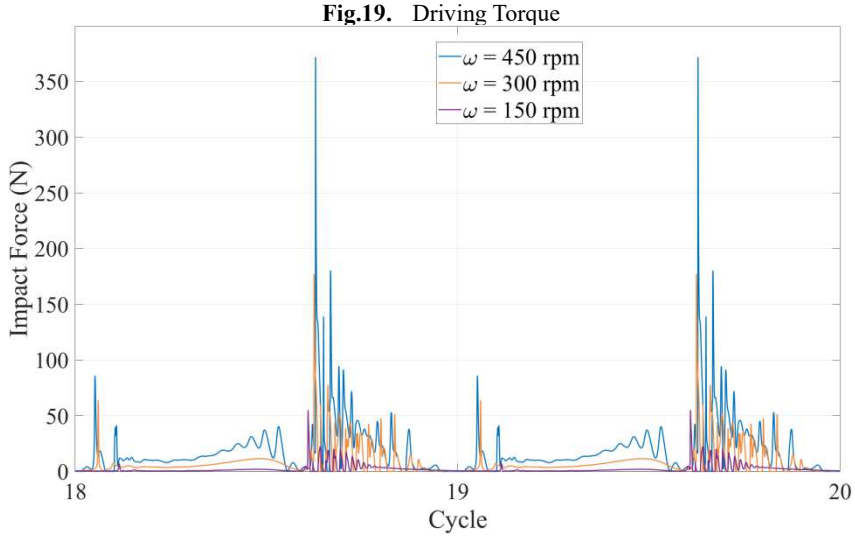


Fig.20. Impact force at clearance A

7.2 Effects of Drive Speed on Revolute Joint Wear Behavior in a High-Frequency Flapping-Wing Mechanism with Joint Clearances

With the revolute joint clearance maintained at 0.3 mm and all other parameters unchanged, clearance A is selected as the representative clearance, and three drive speeds—150, 300, and 450 rpm—are considered to investigate the influence of rotational speed on wear characteristics at the clearance joint and shaft motion. The wear depth, worn bushing profile, and shaft center trajectory

at clearance A under different drive speeds are shown in Figs. 21–23, respectively.

Changes in the bushing profile further reveal the directional preference of wear. Under all three speed conditions, profile deviations are concentrated around [210°,240°], with the most pronounced local deviations and surface irregularities occurring at 450 rpm. This suggests that higher rotational speeds not only increase local wear depth but may also extend the circumferential region affected by heavily loaded contact. The considerable separation between the primary and secondary wear regions suggests that two distinct processes may occur within the clearance joint: primary impacts and contact on the opposite side following rebound. The former governs the principal material loss, while the latter produces less severe additional wear, resulting in a two-region wear pattern with clearly differentiated primary and secondary regions.

As shown in Fig. 23, the shaft center trajectories exhibit repeated crossings and clustering near the clearance boundary, rather than steady, regular circular motion. The trajectories are most densely concentrated in the lower and lower-left regions of the bushing, corresponding to the primary wear locations within [210°,240°]. This indicates that local wear depends not only on the intensity of individual impacts but also closely on the frequency of repeated shaft contact within specific boundary regions. As rotational speed increases, the trajectories become more dispersed, and back-and-forth motion near the boundary becomes more pronounced, indicating more frequent transitions among free motion, impact, and recontact. In other words, the load direction and geometric constraints of the clearance joint determine the regions where contact is most likely to occur, while rotational speed promotes wear accumulation within these regions by altering impact velocity and the number of repeated contacts.

The results also indicate that peak wear does not increase in direct proportion to rotational speed. Local wear intensification is particularly pronounced at 450 rpm, suggesting a nonlinear amplification trend. This may be because high-speed motion simultaneously increases the relative velocity before impact, the frequency of boundary contact, and the magnitude of load fluctuations, causing multiple factors contributing to wear to act together in the primary contact region. Given these characteristics, targeted lubrication, localized surface strengthening, or a replaceable wear-resistant liner in the [210°,240°] region may be more appropriate than relying solely on an overall reduction in rotational speed. Protection of the secondary contact region at [10°,30°] should also be considered to slow profile deterioration in the dominant wear region and clearance growth.

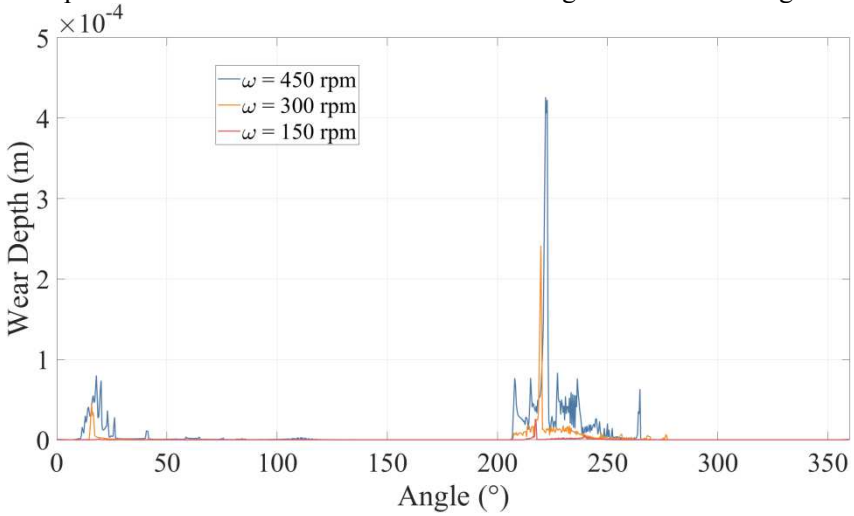
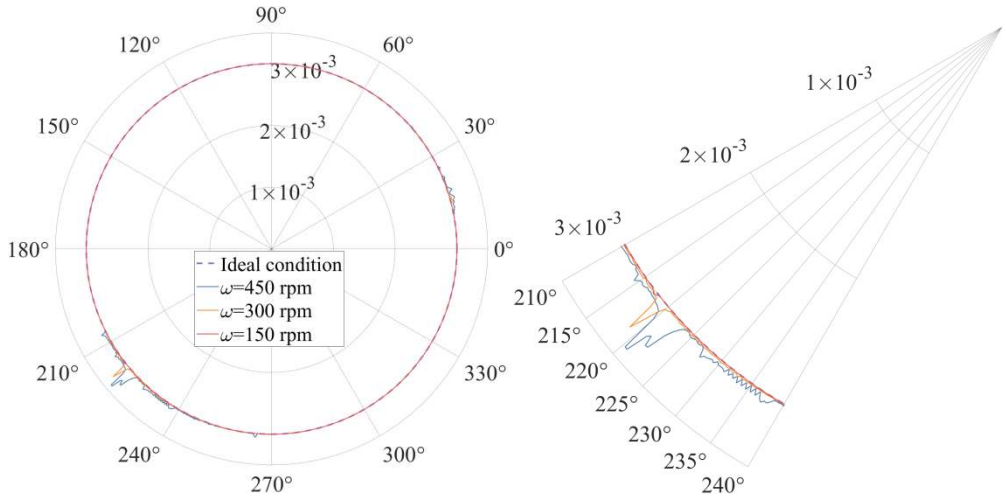


Fig.21. Wear depth at clearance A



(a) Worn surface of the bearing bush **(b)** Enlarged detail

Fig.22. Schematic diagram of bearing wear.

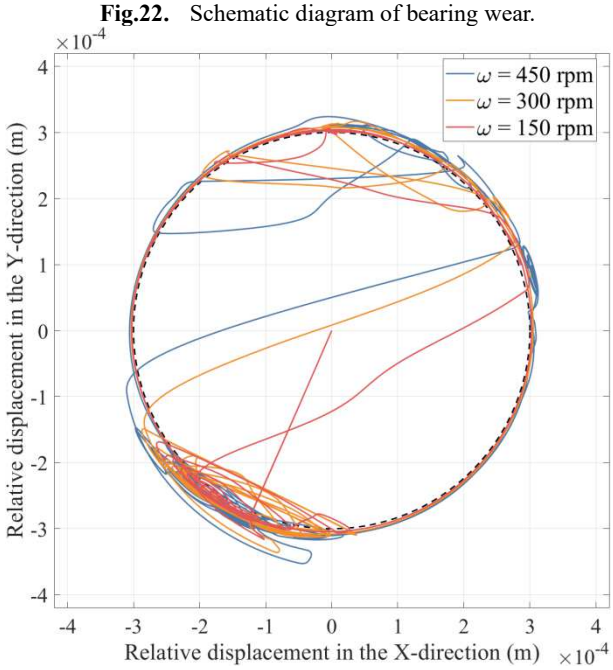


Fig.23. Center trajectory at clearance A

8. Effects of Clearance Size on the Dynamic Response and Revolute Joint Wear Characteristics of a Rigid–Flexible Coupled High-Frequency Flapping-Wing Mechanism with Joint Clearances

8.1 Effects of Clearance Size on the Dynamic Response of a Rigid–Flexible Coupled High-Frequency Flapping-Wing Mechanism with Joint Clearances

To further investigate the influence of revolute joint clearance size on the dynamic response of the rigid–flexible coupled high-frequency flapping-wing mechanism, the input rotational speed is fixed at 450 rpm while all other structural parameters remain unchanged. Four conditions are considered: an ideal clearance-free condition and clearance sizes of 0.1, 0.2, and 0.3 mm. Data from two consecutive cycles during steady operation are selected for comparison. The displacement, velocity, and acceleration responses of the end effector at the main wing tip are presented in Figs. 24, 25, and 26, respectively, while the driving torque and impact force at revolute joint clearance A are shown in Figs. 27 and 28, respectively.

As shown in Fig. 24, the displacement curves under the different conditions largely overlap, with no significant changes in their periods, peak locations, or overall trends. This indicates that clearance size has a relatively limited influence on the primary motion trajectory of the high-

frequency flapping-wing mechanism. However, the enlarged views reveal differences near the displacement minima, indicating that clearance-induced motion errors are concentrated primarily near motion reversal. Compared with displacement, the velocity response is more sensitive to changes in clearance size. Although the maximum velocity remains close to 6 m/s under all conditions, the curves for the mechanisms with clearance exhibit pronounced fluctuations during rapid increases, decreases, and local transitions in velocity. These fluctuations intensify as clearance size increases. This occurs because the shaft alternates among free motion, contact, and separation within the clearance region, introducing a degree of discontinuity into motion transmission.

As shown in Figs. 26–28, acceleration, driving torque, and impact force all exhibit pronounced sensitivity to clearance size. For clearances of 0.1, 0.2, and 0.3 mm, the principal acceleration peaks are approximately 1.0×10^3, 2.3×10^3, and 4.45×10^3 m/s², respectively. The corresponding maximum driving torques are approximately 3, 4.5, and 7.8N·m, while the maximum impact forces are approximately 130, 185, and 370 N. As clearance size increases, both the response peaks and the high-frequency oscillations following the main peaks become substantially more pronounced. Closely spaced secondary impacts are particularly evident at a clearance of 0.3 mm. The principal peaks in acceleration, driving torque, and impact force occur at approximately the same times, indicating that transient loads generated by shaft–bushing impacts can be transmitted along the kinematic chain to the drive, causing simultaneous abrupt changes in the inertial response and drive load.

Further comparison reveals that these peaks recur at intervals of approximately 0.133 s, consistent with one operating cycle at 450 rpm. This indicates that clearance-induced impacts are consistently associated with the motion phase of the high-frequency flapping-wing mechanism, rather than occurring randomly. Moreover, when the clearance increases from 0.2 to 0.3 mm, the peak acceleration and impact force both approximately double, demonstrating pronounced nonlinear amplification of the dynamic response with increasing clearance size. A larger clearance increases the distance over which the shaft moves freely before impact, allowing it to contact the inner bushing surface at a higher relative velocity and weakening the continuous constraint provided by the revolute joint. Therefore, particular attention should be paid to controlling the allowable revolute joint clearance range and optimizing the contact structure and drive parameters during motion reversal to suppress the periodic transmission of impact loads through the mechanism's kinematic chain.

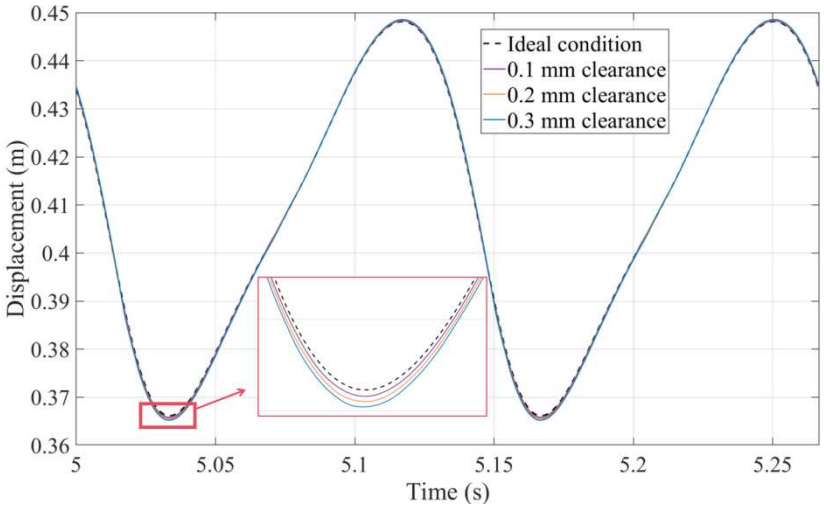


Fig.24. Displacement of the main wing

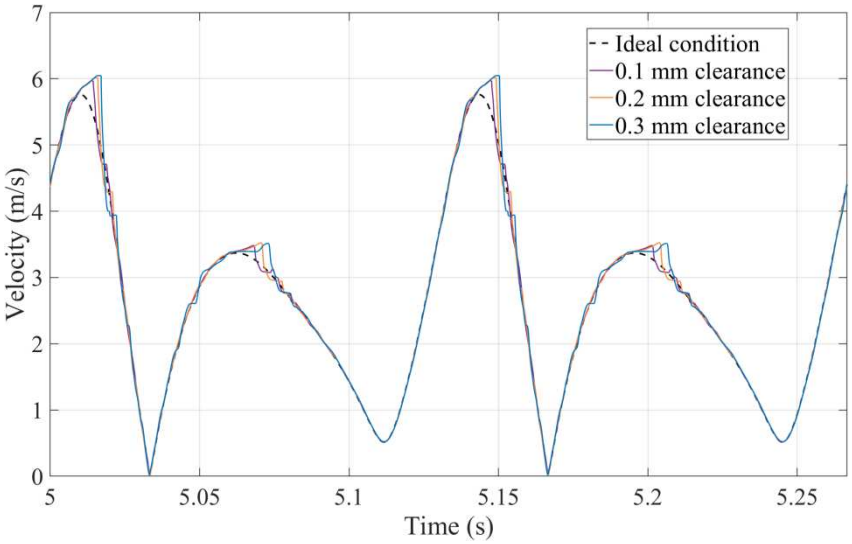


Fig.25. Velocity of the main wing

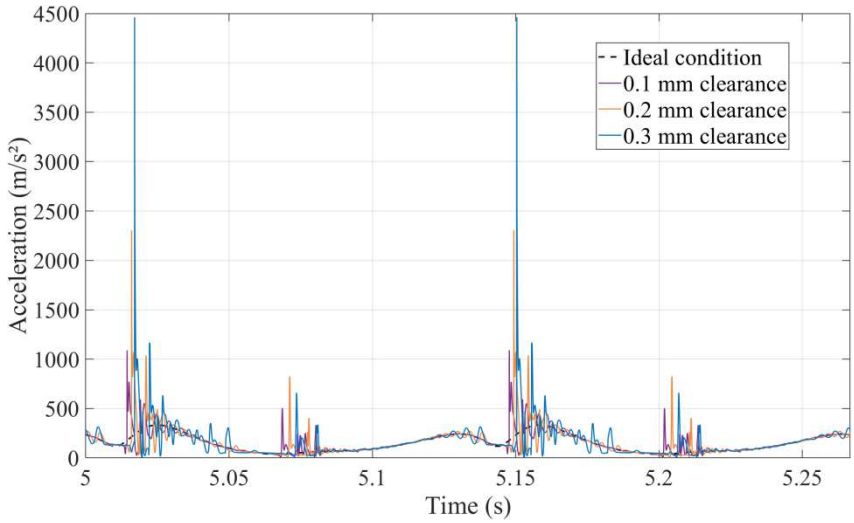


Fig.26. Acceleration of the main wing

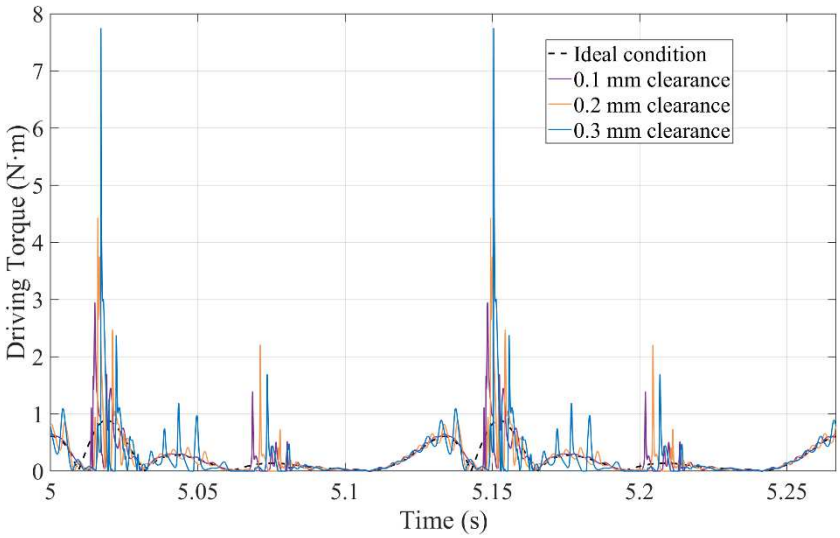


Fig.27. Driving torque at clearance A

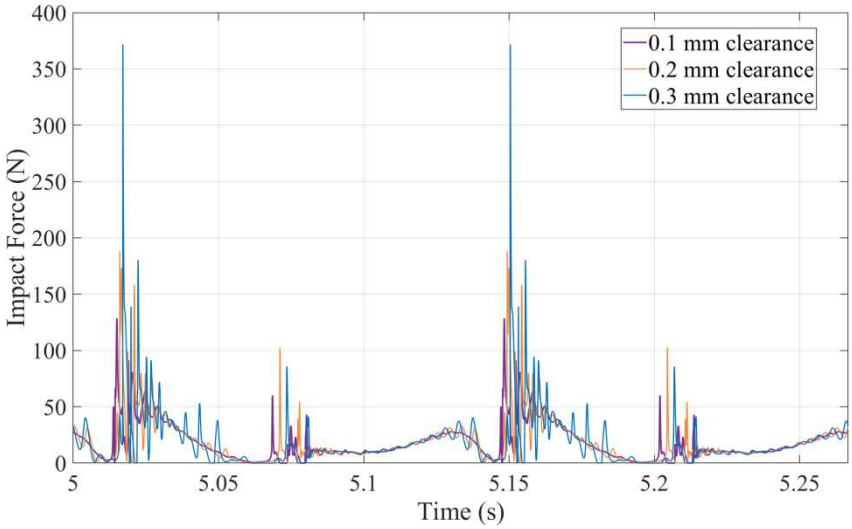


Fig.28. Impact force at clearance A

8.2 Effects of Clearance Size on Revolute Joint Wear Characteristics in a Rigid–Flexible Coupled High-Frequency Flapping-Wing Mechanism with Joint Clearances

With the rotational speed maintained at 450 rpm and all other parameters unchanged, revolute joint A is selected as the representative clearance joint. Three clearance sizes—0.1, 0.2, and 0.3 mm—are considered to investigate the influence of clearance size on the bearing wear distribution and the motion of the shaft and bearing in the high-frequency flapping-wing mechanism. Figure 29 shows that bushing wear is highly localized, with more severe wear concentrated primarily within [210º,260º]. As clearance size increases, both the peak wear depth and the amplitude of fluctuations in the wear curves generally increase. At a clearance of 0.3 mm, the maximum wear peak occurs at approximately 220°, reaching approximately 4.2×10^{-4} m. In addition, the locations of secondary wear regions differ among the clearance conditions, indicating that clearance size affects not only wear severity but also the motion phase and circumferential location at which shaft–bearing impacts occur.

The worn bushing profiles further reflect this nonuniform contact behavior. Relative to the ideal circular profile, pronounced deviations under all three conditions are concentrated in the lower-left region of the bushing. The enlarged views reveal continuous, irregular profile undulations within [210°,255°]. The 0.3 mm clearance produces the largest profile deviations, accompanied by pronounced peaks and local surface irregularities, whereas the profiles for the 0.1 and 0.2 mm clearances remain relatively close to the ideal profile. Local wear does not increase uniformly with clearance size at all angular positions. The curves intersect in some secondary regions, indicating that wear at a specific location is jointly influenced by contact duration, the number of impacts, and instantaneous loads, and cannot be determined by clearance size alone.

The shaft center trajectories in Fig. 31 exhibit pronounced multiple loops, crossings, and clustering near the boundary, indicating that the shaft undergoes various states within the clearance, including free motion, boundary contact, brief sliding, and rebound following impact. As the clearance increases from 0.1 to 0.3 mm, the area covered by the trajectories expands, while the irregularity of the motion paths and the number of back-and-forth movements near the boundary increase substantially. At a clearance of 0.3 mm in particular, the trajectories are highly concentrated near the lower-left boundary, showing close spatial correspondence with the primary wear regions in Figs. 29 and 30. Some trajectories extend slightly beyond the nominal clearance circle, suggesting possible local contact penetration or elastic deformation during impacts. This phenomenon becomes more pronounced at larger clearances.

Taken together, the wear distributions and center trajectories suggest that local bushing damage is governed jointly by the frequency of boundary contact and the intensity of individual impacts. Trajectory clustering near the boundary determines the locations subjected to repeated loading, while increasing clearance size extends the distance over which the shaft moves freely after separating from the bushing, allowing it to attain a higher relative velocity before contacting the inner bushing surface again. Because the kinetic energy before impact is proportional to the square of the relative velocity, the shaft can accumulate more kinetic energy within a larger clearance, increasing energy transfer during impact and further intensifying contact forces and local wear. The

pronounced primary wear peak at a clearance of 0.3 mm indicates that wear may exhibit nonlinear intensification once the clearance becomes sufficiently large. Therefore, clearance design for high-frequency flapping-wing mechanisms should not only limit the nominal clearance size but also focus on the primary contact region within [210°,255°]. Targeted lubrication, localized wear-resistant surface treatment, or optimization of the bushing structure can help distribute repeated impact loads and suppress progressive clearance growth caused by local wear.

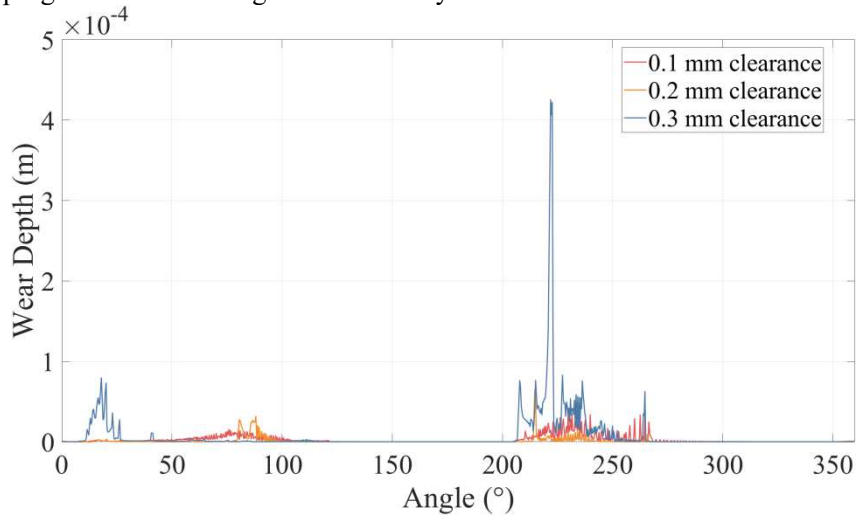
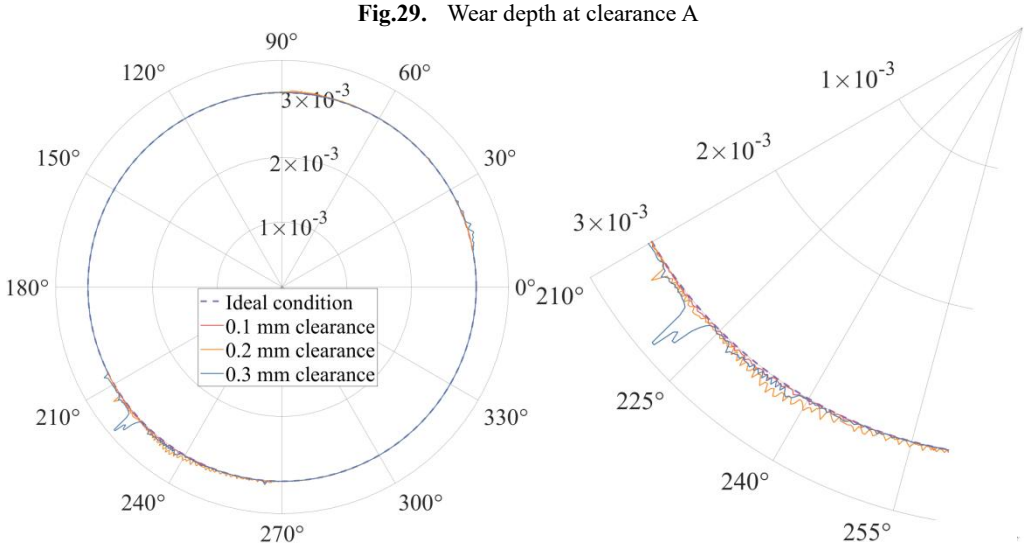


Fig.29. Wear depth at clearance A



(a) Worn surface of the bearing bush **(b)** Enlarged detail

Fig.30. Schematic diagram of bearing wear.

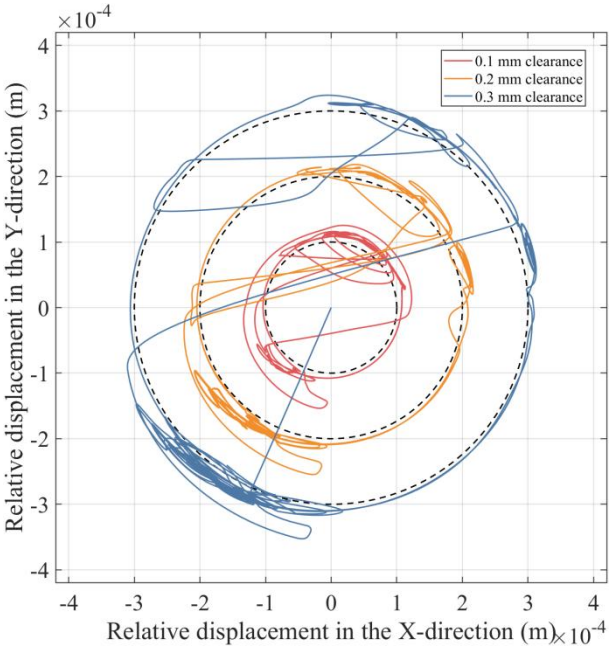


Fig.31. Center trajectory at clearance A

9. Effects of the Number of Clearance Joints on the Dynamic Response and Joint Wear Characteristics of a Rigid–Flexible Coupled High-Frequency Flapping-Wing Mechanism

9.1 Effects of the Number of Clearance Joints on the Dynamic Response of a Rigid–Flexible Coupled High-Frequency Flapping-Wing Mechanism

To further investigate the influence of revolute joint clearances and component flexibility on the dynamic response of the main wing of the high-frequency flapping-wing mechanism, this section examines the effect of the number of clearance joints. Three configurations are considered: clearance A only, clearance B only, and clearances A and B simultaneously. The flexibility of the main wing L_7 is considered, the drive speed is set to 450 rpm, and each clearance is set to 0.3 mm. The mechanism is simulated over two operating cycles. The displacement, velocity, acceleration, and driving torque curves are presented in Figs. 32, 33, 34, and 35, respectively, while the contact forces at the two revolute clearance joints are shown in Figs. 36 and 37.

As shown in Figs. 32–35, increasing the number of clearance joints affects the various responses of the main wing to different degrees. The displacement curves remain generally close to the ideal response, with deviations concentrated primarily near the displacement minima and larger deviations occurring in the dual-clearance configuration. This is mainly because clearance A is connected to the driving arm, allowing the resulting motion deviations to propagate along the kinematic chain to the output, whereas clearance B is connected to the terminal main wing and directly affects its local kinematic constraints. When both clearances are present, their motion deviations combine, causing the main wing displacement to deviate further from the ideal trajectory. As shown in Fig. 33, velocity differences occur primarily near the peaks and during rapid changes. The local fluctuations in the dual-clearance configuration are similar to those in the configuration with clearance A only, indicating that the velocity response does not increase uniformly with the number of clearance joints. In contrast, the changes in acceleration and driving torque are more pronounced. As shown in Fig. 34, the maximum acceleration peak in the dual-clearance configuration is approximately 4,500 m/s², substantially higher than those in either single-clearance configuration. As shown in Fig. 35, the peak driving torque in the dual-clearance configuration approaches 7.8N·m and is accompanied by numerous secondary fluctuations. This may be because contact and separation at the two clearance joints influence one another, intensifying impact-induced velocity changes. Meanwhile, impact loads and additional loads arising from flexible vibration are transmitted along the kinematic chain, increasing the instantaneous acceleration of the main wing

and the torque demand at the drive.

As shown in Figs. 36 and 37, the maximum impact forces at both clearances A and B are substantially higher in the dual-clearance configuration than in the corresponding single-clearance configurations. Specifically, the maximum impact force at clearance A increases from approximately 190 to 370 N, while that at clearance B increases from approximately 80 to 270 N. This indicates that introducing an additional clearance affects not only the contact state at the newly introduced clearance joint but also the impact response at the existing one. Because clearance A is located on the driving-arm side, its impact disturbances can influence the main wing motion and the relative motion at clearance B through the kinematic chain. Changes in the contact state at clearance B, in turn, alter load transmission to the drive. These interactions may increase local contact velocities and impact loads. However, some secondary impact peaks at clearance A decrease in the dual-clearance configuration, indicating that the effects of multiple clearances are not a simple addition of individual impacts but involve a redistribution of contact timing and loads. Thus, under the present operating conditions, the combined action of the two clearances substantially amplifies the principal impact peaks. Even when the overall main wing displacement changes only slightly, the mechanism may still experience considerably greater transient dynamic loads.

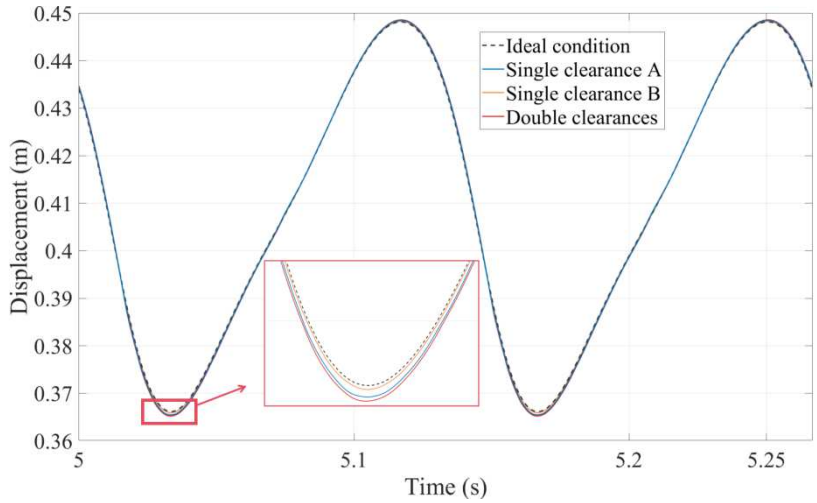


Fig.32. Displacement of the main wing

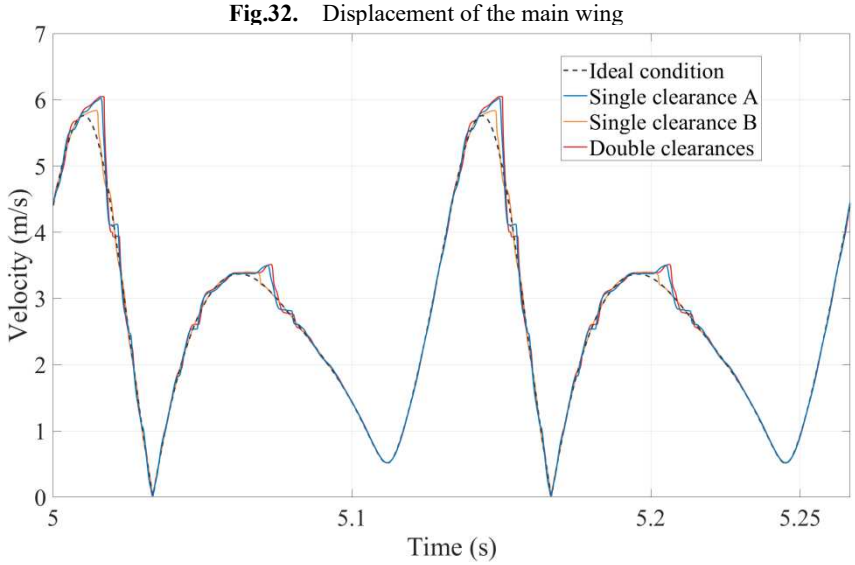


Fig.33. Velocity of the main wing

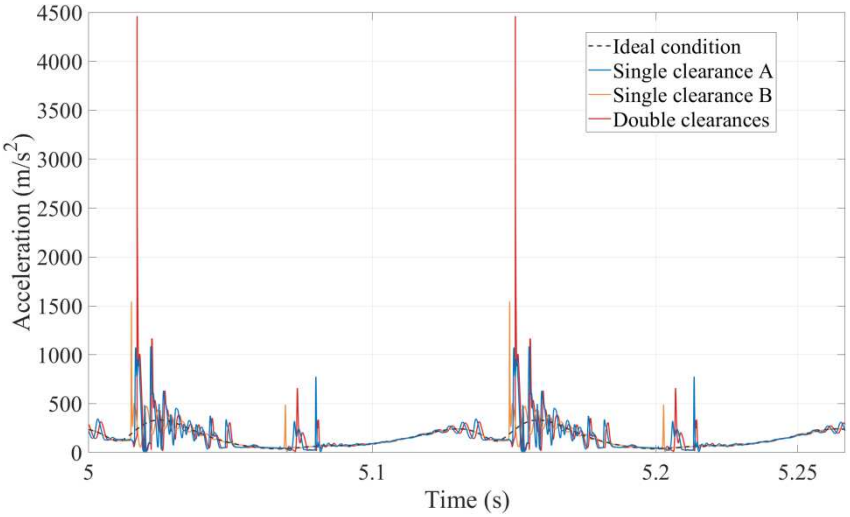


Fig.34. Acceleration of the main wing

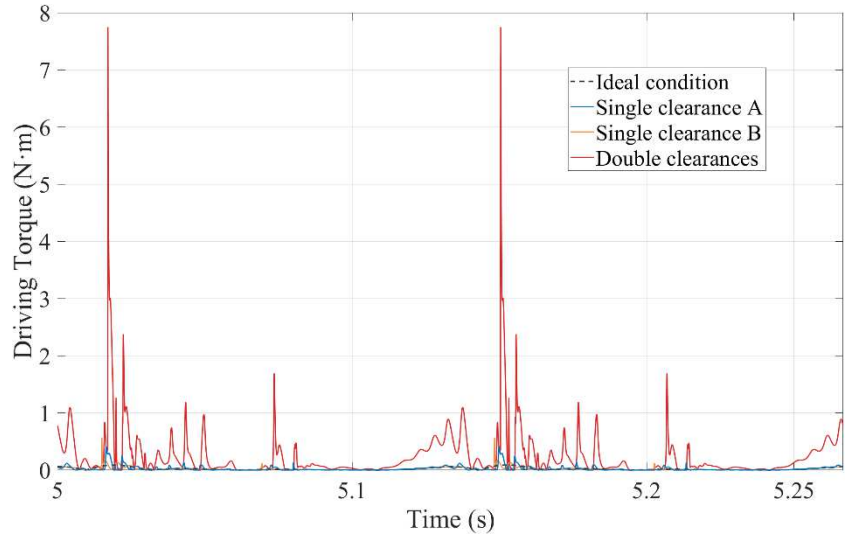


Fig.35. Driving torque

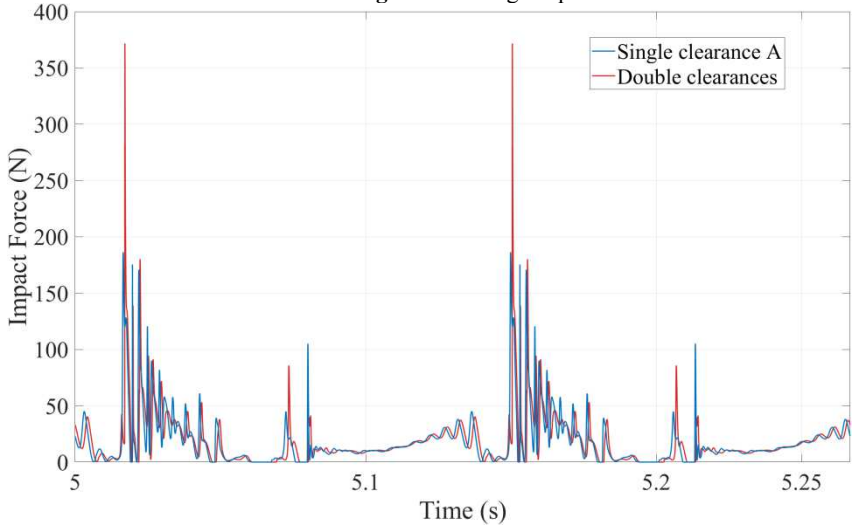


Fig.36. Impact force at clearance A

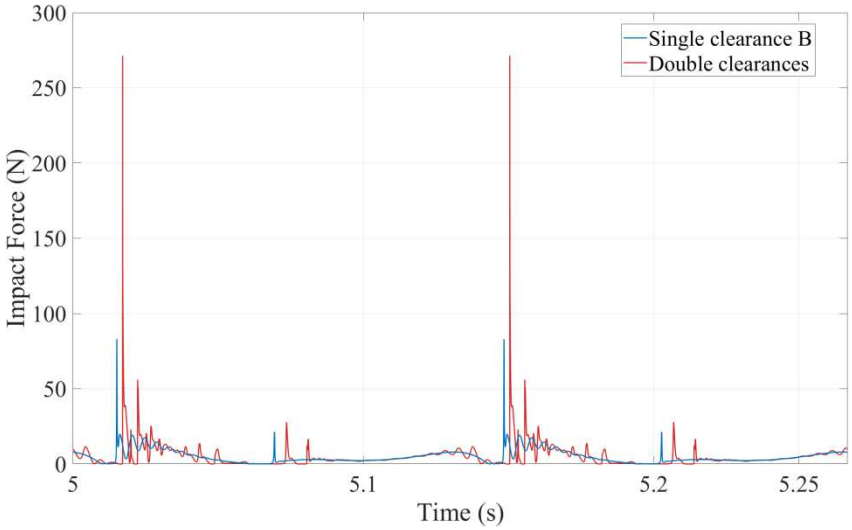


Fig.37. Impact force at clearance B

9.2 Effects of the Number of Clearance Joints on Revolute Joint Wear Characteristics in a Rigid–Flexible Coupled High-Frequency Flapping-Wing Mechanism

This section investigates the wear characteristics of the shafts at revolute clearance joints in the rigid–flexible coupled high-frequency flapping-wing mechanism with different numbers of clearance joints. The clearance size and drive speed are set to 0.3 mm and 450 rpm, respectively. Figures 38 and 39 present the wear depths on the shaft surfaces, Figs. 40 and 41 show the worn shaft profiles, and Figs. 42 and 43 illustrate the shaft center trajectories at the two revolute clearance joints.

As shown in Figs. 38–41, the maximum wear depths at both clearances A and B increase substantially in the dual-clearance configuration compared with the single-clearance configurations, and the locations of concentrated wear also change. At clearance A, wear is primarily distributed within [210°,270°]. In the single-clearance configuration, the larger wear peaks are concentrated around [240°,250°], whereas the dual-clearance configuration exhibits a pronounced peak at approximately 220°, with a maximum wear depth of approximately 4.2×10^{-4} m. Appreciable wear also occurs around 10°–30°. At clearance B, the primary wear region lies within [250°,300°]. In the dual-clearance configuration, the maximum wear depth at approximately 260° reaches 9.4×10^{-5} m, exceeding the approximately 3.2×10^{-5} m observed in the single-clearance configuration. Local wear near 65° also increases in the dual-clearance configuration. As shown in Figs. 40 and 41, deeper depressions appear in the shaft surface profiles at the locations corresponding to these wear peaks in the dual-clearance configuration. This indicates that the combined action of the two clearances not only increases local material loss but also alters the circumferential wear distribution. This may be because the additional clearance changes the kinematic constraints and load transmission within the mechanism, altering the contact locations, local contact pressures, and cumulative relative sliding between the shafts and bushings, thereby producing wear accumulation in different angular regions.

As shown in Figs. 42 and 43, the overall outer envelopes of the shaft center trajectories are similar under the two configurations, but the internal motion paths and local back-and-forth movements differ considerably. The trajectories at clearance A are relatively dense in the lower-left region, while those at clearance B exhibit concentrated deviations in the lower region. These locations approximately correspond to the primary wear regions at the two clearance joints. Because clearance A is connected to the driving arm, its motion disturbances can propagate along the kinematic chain to the output. Clearance B is connected to the terminal main wing, and changes in its contact state can, in turn, affect the transmission of main wing loads back to the drive. When both clearances are present, these interactions, together with the flexible deformation of the main wing, alter the local contact processes. This may concentrate repeated contact and frictional action at certain locations, thereby increasing wear depth. In the dual-clearance configuration, the maximum wear depth at clearance A is substantially greater than that at clearance B, possibly because their different locations result in different local loads and sliding histories. Thus, the influence of the number of clearance joints on wear is reflected not only in changes in maximum wear depth but also in shifts in wear locations and changes in wear concentration. Wear severity

therefore cannot be assessed solely from the degree of crossing in the shaft center trajectories.

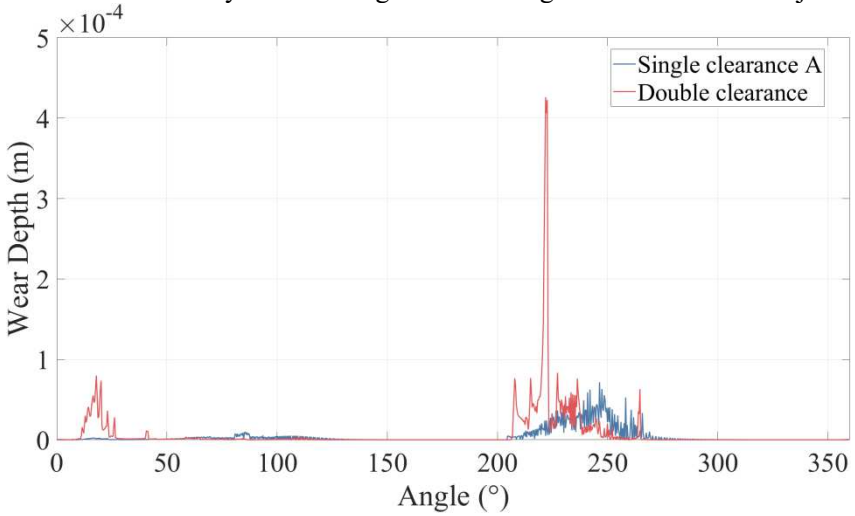


Fig.38. Wear depth at clearance A

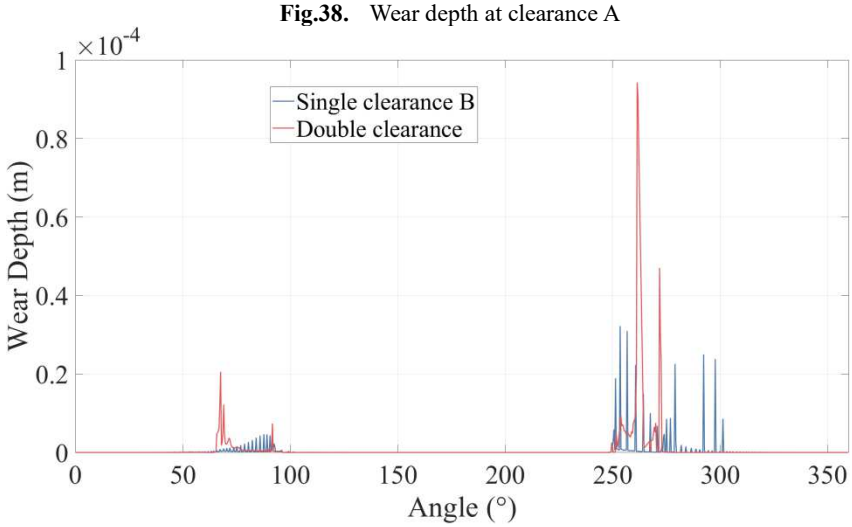
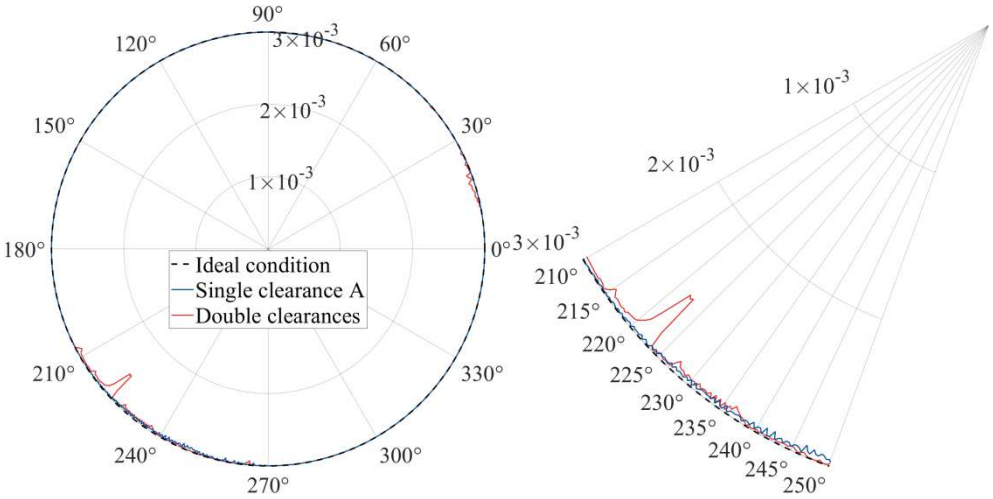
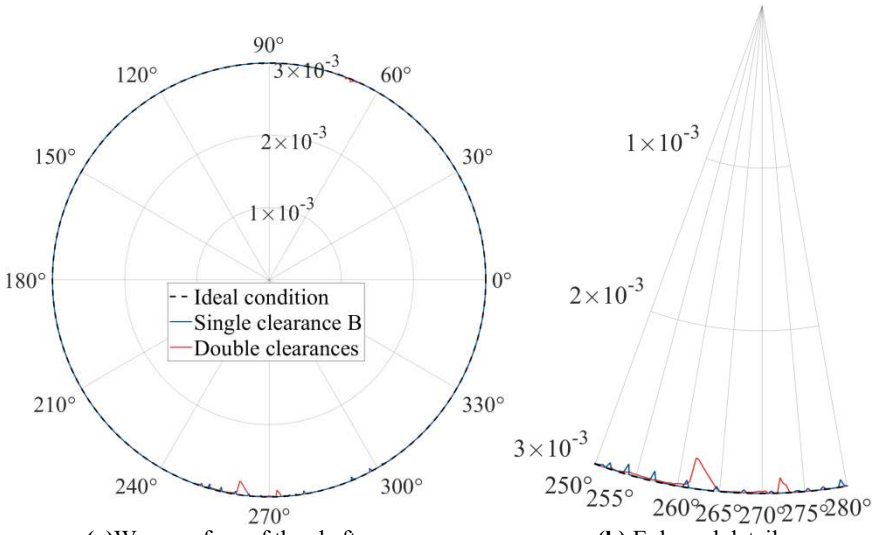


Fig.39. Wear depth at clearance B



(a) Worn surface of the shaft **(b)** Enlarged detail

Fig.40. Schematic diagram of shaft wear at clearance A



(a) Worn surface of the shaft **(b)** Enlarged detail

Fig.41. Schematic diagram of shaft wear at clearance B

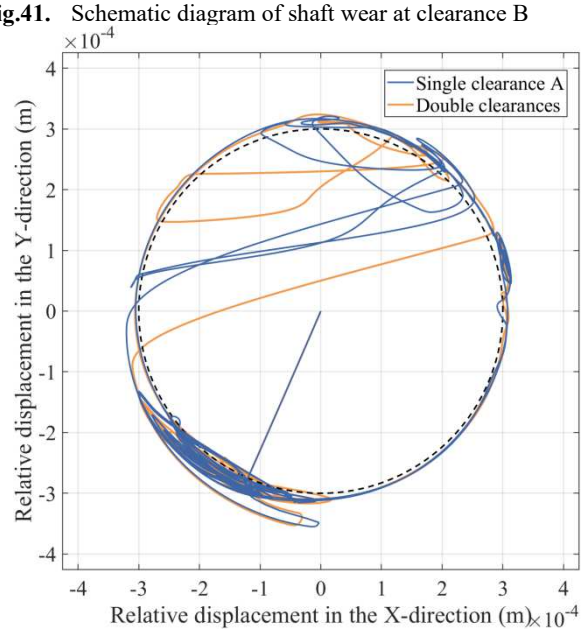


Fig.42. Center trajectory at clearance A

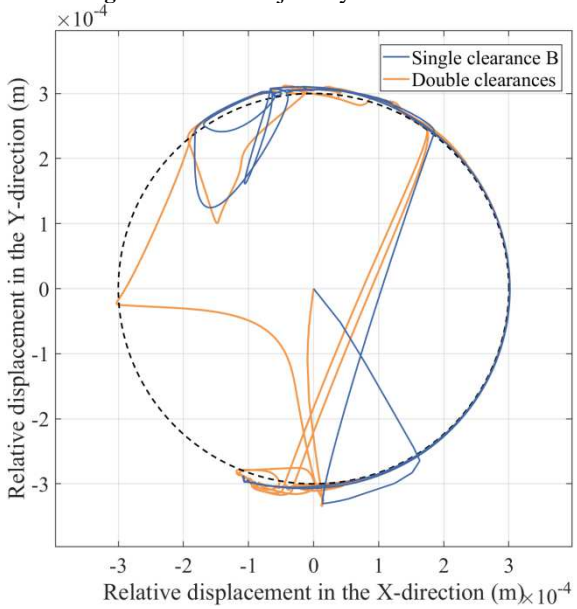


Fig.43. Center trajectory at clearance B

10. Conclusions

A rigid–flexible coupled dynamic framework incorporating revolute-joint clearance and wear evolution was developed for a high-frequency flapping-wing mechanism. By combining clearance-joint contact dynamics, ANCF-based flexible-body modeling, and Archard wear prediction, the framework was used to examine the coupled effects of component flexibility, clearance size, drive speed, and the number of clearance joints. The main conclusions are as follows:

(1) Revolute-joint clearance has a limited effect on the overall displacement trajectory of the main wing but substantially increases local velocity fluctuations, acceleration peaks, driving torque, and impact force. These effects become more pronounced as the clearance size and drive speed increase.

(2) Structural flexibility significantly modifies clearance-induced impact behavior. Elastic deformation and subsequent energy release alter the relative motion and contact state between the shaft and bushing. As a result, flexibility may either amplify or mitigate individual impacts depending on the phase of motion, although pronounced peak responses are observed under the operating conditions considered in this study.

(3) Component flexibility also changes the spatial distribution of joint wear by modifying contact location, local load, and relative sliding. Consequently, concentrated wear may become more severe even when the overall shaft-center trajectory changes only moderately.

(4) The combined analysis reveals pronounced coupling among clearance, flexibility, and wear in the high-frequency flapping-wing mechanism. A rigid-body dynamic model alone is therefore insufficient to accurately describe its actual operating behavior. Accordingly, flexible component parameters and clearance characteristics should be considered together during mechanism design and optimization to improve motion accuracy and service reliability.

Funding: This research received no external funding.

Data Availability Statement: The data used to support the results of this research are included in this paper.

Conflicts of Interest: Authors declare that they have no conflict of interest.

References

[1] SONG G, QIAN S, ZHANG T, et al. Dynamic modeling and stepwise parameter identification of a 4-4R rigid-flexible coupled mechanism with inertial measurement unit [J]. Nonlinear Dynamics, 2026, 114(10).

[2] GUO X, YANG X, LIU F, et al. Dynamic analysis of the flexible hub-beam system based on rigid-flexible coupling mechanism [J]. Proceedings of the Institution of Mechanical Engineers Part K-Journal of Multi-Body Dynamics, 2020, 234(3): 536–45.

[3] LINJING X, CHENGZHE L, FANGPING Y, et al. Dynamics research and chaos identification of rigid-flexible coupling multi-link mechanism with irregular wear clearances [J]. Nonlinear Dynamics, 2023, 111(14): 12983–3015.

[4] SUN G, ZHANG H, WU J, et al. Study on the progressive collapse resistance of hybrid rigid-flexible boundary cable net structures [J]. Thin-Walled Structures, 2026, 219.

[5] WEI Z, WANG Z, LI D, et al. Rigid-flexible coupling dynamic modelling and dynamic accuracy analysis of planar cam four-bar mechanism with multiple clearance joints [J]. Proceedings of the Institution of Mechanical Engineers Part K-Journal of Multi-Body Dynamics, 2024, 238(3): 421–44.

[6] LI Y, WAN X, MENG K, et al. Study on the Influence of Lubrication Effect on Nonlinear Dynamics of Rigid-Flexible Coupling Mechanisms with Clearance [J]. Mechanics of Solids, 2025, 60(1): 484–523.

[7] WANG X, WANG H, ZHAO J, et al. Rigid-Flexible Coupling Dynamics Modeling of Spatial Crank-Slider Mechanism Based on Absolute Node Coordinate Formulation [J]. Mathematics, 2022, 10(6).

[8] LI J, CHANG Y, CHEN G, et al. Research of rigid-flexible coupling dynamics model for riser-LMRP/ BOPs-wellhead system [J]. Ocean Engineering, 2024, 291.

[9] ZHANG C, JIANG H. Rigid-Flexible Modal Analysis of the Hydraulic 6-DOF Parallel Mechanism [J]. Energies, 2021, 14(6).

[10] LOBONTIU N. Dynamic compliance-based matrix model and analysis of planar serial mechanisms with rigid links and flexible hinges: A parallelogram design [J]. Mechanism and Machine Theory, 2026, 226.

[11] LAI J, YANG S. Flow-induced vibration of a flexible tube with squeeze film in an otherwise rigid tube array subjected to cross-flow [J]. Nonlinear Dynamics, 2025, 113(6): 5023–39.

[12] ZHENG Y, YANG Y, WU R, et al. Dynamic analysis of a hybrid compliant mechanism with flexible central chain and cantilever beam [J]. Mechanism and Machine Theory, 2021, 155.

[13] NIU J, MENG K, AN M, et al. Dynamic Response and Nonlinear Characteristic Analysis of Rigid-Flexible Coupling Mechanism with Lubricated Revolute Clearance and Prismatic Clearance [J]. Lubricants, 2025, 13(4).

[14] LI Y, CHEN G, SUN D, et al. Dynamic analysis and optimization design of a planar slider-crank mechanism with flexible components and two clearance joints [J]. Mechanism and Machine Theory, 2016, 99: 37–57.

[15] HOU J, YAO G, HUANG H. Dynamic Analysis of a Spatial Mechanism Including Frictionless Spherical Clearance Joint With Flexible Socket [J]. Journal of Computational and Nonlinear Dynamics, 2018, 13(3).

[16] XIN Y, ZHU J, MENG K, et al. Nonlinear dynamics study of hybrid mechanism considering three-dimensional revolute joint clearance [J]. Nonlinear Dynamics, 2025, 113(13): 16245–75.
[17] YI Z, TIAN Z, HU Z, et al. Macro-micro coupled nonlinear dynamic analysis of thin-walled spiral bevel gear transmission systems with response-dependent contact evolution [J]. Mechanism and Machine Theory, 2026, 228.
[18] JIA Y, HU X, DAI H, et al. Rigid-flexible coupling dynamics of hybrid robots with joint clearances: analysis, sensitivity screening, and model order reduction [J]. Nonlinear Dynamics, 2026, 114(9).
[19] ALI J, SHAVER G, BAJAJ A. Modeling and analysis of unilateral rigid impacts in a universal joint with clearance [J]. Nonlinear Dynamics, 2026, 114(6).
[20] DOU Q, LUO H, SONG Y, et al. Failure analysis of diesel engine connecting rod Big-End bearing wear considering coupled clearance lubrication joints [J]. Engineering Failure Analysis, 2025, 169.
[21] ZHAO B, DAI X, ZHANG Z, et al. Numerical study of parametric effects on joint wear in the flexible multibody systems with different flexibilities and clearance sizes [J]. Proceedings of the Institution of Mechanical Engineers Part J-Journal of Engineering Tribology, 2014, 228(8): 819–35.
[22] EBRAHIMI S, SALAHSHOOR E, MORADI S. Vibration performance evaluation of planar flexible multibody systems with joint clearance [J]. Journal of the Brazilian Society of Mechanical Sciences and Engineering, 2017, 39(12): 4895–909.
[23] WANG H, WANG Z, ZUO K, et al. Wear analysis of small-end bearing of diesel engine under multi-clearance lubrication [J]. Tribology International, 2026, 221.
[24] LU Y, JIA H, YI J, et al. Wear characteristics and nonlinear analysis of rigid-flexible coupling rudder actuator with irregular wear clearance [J]. Communications in Nonlinear Science and Numerical Simulation, 2026, 160.
[25] WANG C, LE T, HUYNH N. Optimal rigid-flexible dynamic of space slider-crank mechanism with clearance joints [J]. Sadhana-Academy Proceedings in Engineering Sciences, 2023, 48(2).
[26] LU Y, LI X, XIE Z, et al. Rigid-flexible coupling modeling and nonlinear analysis of rudder actuator with lubrication clearance [J]. Mechanical Systems and Signal Processing, 2026, 247.
[27] ERKAYA S, DOGAN S. A comparative analysis of joint clearance effects on articulated and partly compliant mechanisms [J]. Nonlinear Dynamics, 2015, 81(1-2): 323–41.
[28] HU L, LI B, WANG Z, et al. Analysis and evaluation of multi-state wear mechanism of elastic-flexible thin-walled bearings [J]. Tribology International, 2025, 202.
[29] SONG N, PENG H, KAN Z. Nonsmooth strategy for rigid-flexible multibody system considering different types of clearance joints and lubrication [J]. Multibody System Dynamics, 2022, 55(3): 341–74.
[30] ZHANG H, LUO Z, YAO S, et al. Dynamic analysis and experimental study of spatial rigid-flexible coupling mechanism with frictional clearance joints [J]. Journal of Sound and Vibration, 2026, 644.
[31] LI B, WANG M, GANTES C, et al. Modeling and simulation for wear prediction in planar mechanical systems with multiple clearance joints [J]. Nonlinear Dynamics, 2022, 108(2): 887–910.
[32] WANG H, PENG Y, WANG Z, et al. Crankshaft misalignment effect on bearing tribo-dynamics under multi-clearance lubrication [J]. International Journal of Mechanical Sciences, 2025, 307.
[33] TANG L, LIU J. Frictional contact analysis of sliding joints with clearances between flexible beams and rigid holes in flexible multibody systems [J]. Multibody System Dynamics, 2020, 49(2): 155–79.
[34] YIN Y, XU K, NIE H, et al. Dynamics Analysis of Spatial Landing-Gear Mechanism with Hinge Clearance and Axis Deviation [J]. Journal of Aircraft, 2021, 58(1): 30–42.
[35] LIU S, CUI Y, XING M, et al. A general tribo-dynamic model for lubricated clearance joints in spatial multibody systems [J]. Scientific Reports, 2025, 15(1).
[36] CHEN Z, QIAN M, SUN F, et al. A quantitative analysis method for contact force of mechanism with a clearance joint based on entropy weight and its application in a six-bar mechanism [J]. Chinese Physics B, 2022, 31(4).
[37] SU Y, ZHANG W, ZHANG J, et al. Research on the dynamic properties of the ball bearing considering cage flexibility under acceleration conditions: ball skidding behavior and cage whirl mechanism [J]. Mechanical Systems and Signal Processing, 2026, 257.
[38] QUESTA H, MOHAMMADPOUR M, THEODOSSIADES S, et al. Tribodynamic Modelling of High-Speed Rolling Element Bearings in Flexible Multi-Body Environments [J]. Machines, 2023, 11(1).
[39] LANKARANI H M, NIKRAVESH P E. Continuous contact force models for impact analysis in multibody systems [J]. Nonlinear Dynamics, 1994, 5(2): 193–207.
[40] AMBRóSIO J A C. Impact of Rigid and Flexible Multibody Systems: Deformation Description and Contact Models [M]//SCHIEHLEN W, VALáŠEK M. Virtual Nonlinear Multibody Systems. Dordrecht; Springer Netherlands. 2003: 57–81.
[41] ZHOU S, ORR A, HYUN N, et al. Importance of Translational Velocity for Bird-scale Flapping Wing Vehicles Incapable of Hovering; proceedings of the 2024 International Conference on Intelligent Robots and Systems, Abu Dhabi, U ARAB EMIRATES, F Oct 14–18 2024, 2024 [C]. 2024.